

# **Observations of traveling ionospheric disturbances driven by gravity waves from sources in the upper and lower atmosphere**

Paul Prikryl<sup>1</sup>, David R. Themens<sup>1,2</sup>, Jaroslav Chum<sup>3</sup>, Shibaji Chakraborty<sup>4</sup>, Robert G. Gillies<sup>5</sup>, James M. Weygand<sup>6</sup>

<sup>1</sup>Physics Department, University of New Brunswick, Fredericton, NB, Canada

<sup>2</sup>School of Engineering, University of Birmingham, Birmingham, UK

<sup>3</sup>Institute of Atmospheric Physics CAS, Prague, Czech Republic

<sup>4</sup>Center for Space Science and Engineering Research, Virginia Tech, Blacksburg, VA, USA

<sup>5</sup>Department of Physics and Astronomy, University of Calgary, Calgary, AB, Canada

<sup>6</sup>Earth, Planetary, and Space Sciences, University of California, Los Angeles, CA, USA

*Correspondence to:* Paul Prikryl (paul.prikryl@unb.ca)

## **Abstract**

Traveling ionospheric disturbances (TIDs) are observed by the Super Dual Auroral Radar Network (SuperDARN), the Poker Flat Incoherent Scatter Radar (PFISR), the multipoint and multifrequency continuous Doppler sounders, and the GNSS total electron content (TEC) mapping technique. PFISR measures electron density altitude profiles, from which TIDs are obtained by a filtering method to remove background densities. SuperDARN observes the ionospheric convection at high latitudes and TIDs modulating the ground scatter power. The Doppler sounders at mid latitudes can determine TID propagation velocities and azimuths. The aim of this study is to attribute the observed TIDs to atmospheric gravity waves generated in the lower thermosphere at high latitudes, or gravity waves generated by mid-latitude tropospheric weather systems. The solar wind-magnetosphere-ionosphere-thermosphere coupling modulates the dayside ionospheric convection and currents that generate gravity waves driving equatorward propagating medium to large scale TIDs. The horizontal equivalent ionospheric currents are estimated from the ground-based magnetometer data using an inversion technique. At high latitudes, TIDs observed in the detrended TEC maps are dominated by equatorward TIDs pointing to auroral sources. At mid to low latitudes, the azimuths of TIDs vary, indicating sources in the troposphere. The cases of eastward to southeastward propagating TIDs that are observed in the detrended TEC maps and by the HF Doppler sounders in Czechia are attributed to gravity waves that were likely generated by geostrophic adjustment processes and shear instability in the intensifying low-pressure systems.

## 1. Introduction

The relationship between atmospheric gravity waves (AGWs) and traveling ionospheric disturbances (TIDs) has been well established (Hocke and Schlegel, 1996). The theory governing the propagation and effects of AGWs in the ionosphere was developed by Hines (1960) and their ionospheric sources have been recognized (Chimonas, 1970; Chimonas and Hines, 1970; Testud, 1970; Richmond, 1978). Global propagation of medium- to large-scale GWs/TIDs has been linked to auroral sources (Hunsucker, 1982; Hajkowicz, 1991; Lewis *et al.*, 1996; Balthazor and J., 1997). The Worldwide Atmospheric Gravity-wave Studies (WAGS) program (Crowley and Williams, 1988; Williams *et al.*, 1993) showed that large-scale TIDs originate in auroral latitudes. TIDs generated by AGWs originating in the lower atmosphere come from a variety of sources, including tropospheric weather systems (Bertin, Testud and Kersley, 1975; Bertin *et al.*, 1978; Waldock and Jones, 1987; ~~Oliver *et al.*, 1997~~; Nishioka *et al.*, 2013; Azeem *et al.*, 2015), solar flares (Zhang *et al.*, 2019), total solar eclipses (Zhang *et al.*, 2017; Mrak *et al.*, 2018), the polar vortex (Frissell *et al.*, 2016), volcanic eruptions, earthquakes, and tsunamis (Yu, Wang and Hickey, 2017; Nishitani *et al.*, 2019; Themens *et al.*, 2022). Becker *et al.* (2022) performed simulations focusing on multi-step vertical coupling by primary, secondary, and higher-order gravity waves of wintertime thermospheric gravity waves and compared them with observed perturbations of total electron content. They demonstrated that gravity waves generated from lower altitudes can propagate equatorward. Further modelling and observations related gravity waves to polar vortex sources (Bossert *et al.*, 2020; 2022; Becker *et al.*, 2022; Vadas *et al.*, 2023).

The solar wind coupling to the dayside magnetosphere (Dungey, 1961, 1995) generates variable electric fields that map to the ionosphere driving the  $E \times B$  ionospheric convection and currents. The Joule heating due to the ionospheric currents of in the lower thermosphere is a source of equatorward propagating AGWs, which in turn drive TIDs (e.g., Prikryl *et al.*, 2022). The electric fields transmitted to the low latitude ionosphere in the magnetosphere-ionosphere current circuit (Kikuchi and Hashimoto, 2016) play a role in generating TIDs through ion-neutral interactions (Nishitani *et al.*, 2019) and an electrodynamic instability mechanism (Kelley *et al.*, 2023). In the troposphere, convection is often a source of gravity waves propagating into the upper atmosphere driving TIDs (e.g., Azeem, 2021; and references therein). However, large amplitude gravity waves generated in the troposphere by geostrophic adjustment processes and shear

**Formatted:** Font: (Default) Times New Roman, (Asian) Times New Roman

**Formatted:** Font: (Default) Times New Roman, (Asian) Times New Roman

**Formatted:** Font: (Default) Times New Roman, (Asian) Times New Roman

**Formatted:** Font: (Default) Times New Roman, (Asian) Times New Roman

**Formatted:** Font: (Default) Times New Roman, (Asian) Times New Roman, 12 pt

**Formatted:** Font color: Text 1, English (Canada)

**Formatted:** Font: (Default) Open Sans, (Asian) Open Sans, 10.5 pt, Font color: Custom Color(RGB(28,29,30))

instability (Klostermeyer, 1977; Uccellini and Koch, 1987) have been rarely considered to drive TIDs.

We present observations of TIDs by radars, Doppler sounders and the GNSS TEC mapping technique. The aim of this study is to attribute the observed TIDs to sources in the upper (Section 3), and the lower (Section 4) atmosphere. These observations show that AGWs provide both downward and upward vertical coupling of the ionosphere and neutral atmosphere.

## 2. Data sources and methods

Advanced Modular Incoherent Scatter Radar (AMISR) technology with its unique steering and beam-forming capabilities has been described by Heinselman and Nicolls (2008) and has been used to investigate gravity wave propagation (Nicolls and Heinselman, 2007; Vadas and Nicolls, 2008). The Poker Flat Incoherent Scatter Radar (PFISR) located at the Poker Flat Research Range (65.1°N, 147.5°W) near Fairbanks, Alaska running a 7-beam mode (Heinselman and Nicolls, 2008) measured altitude profiles of the electron densities. To retrieve TIDs, background densities are removed by applying Savitzky-Golay filter (Press and Teukolsky, 1990).

The multi-point and multi-frequency continuous HF Doppler sounding system operating in the Czech Republic is described by Chum et al. (2021). It consists of three transmitting sites Tx1, Tx2, and Tx3 distributed in the western part of the Czech Republic (Tx1: 50.528°N, 14.567°E; Tx2: 49.991°N, 14.538°E; Tx3: 50.648°N, 13.656°E) and receiver Rx located in Prague (50.041°N, 14.477°E). Radio waves at different frequencies (3.59, 4.65 and 7.05 MHz) are transmitted from each site. First, the time evolution of power spectral densities ~~–~~ Doppler shift spectrograms ~~→~~ are computed for each signal and the maximum of power spectral density (characteristic Doppler shift) is found with selected time resolution suitable for the TIDs/GWs analysis (30 or 60 s). TID/GW cause movement of plasma and therefore the Doppler shift. The propagation velocities and azimuths are then determined from the time delays between the Doppler shifts recorded for different transmitter-receiver pairs and expected distances of the reflection points in the ionosphere are determined by two- or three- dimensional methods described in detail by Chum and Podolská (2018) and Chum et al. (2021).

SuperDARN constitutes a globally distributed HF Doppler radar network, operational within the frequency range of 8 to 18 MHz, encompassing both the northern and southern hemispheres across various latitudinal bands, including middle, high, and polar zones. Each radar within this network measures the line-of-sight (LoS) component of the drift velocity associated with ionospheric plasma irregularities (Chisham et al., 2007; Nishitani et al., 2019). The observations from SuperDARN encompass two principal forms of backscatter, namely, ionospheric scatter and ground scatter. Ionospheric scatter is generated when a transmitted signal is scattered from ionospheric irregularities. In the case of ground scatter, due to the significant daytime vertical refractive index gradient, the propagation rays alter their trajectory towards the ground, scattering from surface roughness before returning along the same path to the radar. Prior research has demonstrated the utility of both scatter types in studies of pulsed ionospheric flows (PIFs) (McWilliams, Yeoman and Provan, 2000; Prikryl *et al.*, 2002) and TIDs (Samson et al., 1990). In this study, we use line-of-sight (LoS) Doppler velocities and ground scatter observations to characterize TIDs, with supplementary support from ionospheric convection maps available at the SuperDARN Virginia Tech (VT) website ([vt.superdarn.org](http://vt.superdarn.org)) to validate their sources.

The Spherical Elementary Current System (SECS) inversion technique (Amm and Viljanen, 1999) is used to estimate horizontal equivalent ionospheric currents (EICs) from the ground-based magnetic field measurements by several arrays of magnetometers in the North American sector and the western Greenland (Weygand et al., 2011; their Table 1). For each of these magnetometers the quiet-time background is subtracted from the measured field to give the disturbance component which determines the EICs (Weygand et al., 2011).

Global Navigation Satellite System (GNSS) data for this were gathered from the same global networks of GNSS receivers used in Themens et al. (2022), which constitute 5200-5800 stations, depending on the period. Examples of the GNSS station distribution in the two local domains can be viewed in Fig. S1 in the Supplement. Using the phase leveling and cycle slip correction method outlined by Themens et al. (2013), the LoS total electron content (TEC) is determined from the differential phase and code measurements of these systems. As detailed in Themens et al. (2015), the satellite biases are acquired from the Center for Orbit Determination in Europe (CODE, [ftp://ftp.aiub.unibe.ch/](http://ftp.aiub.unibe.ch/)) and receiver biases are determined.

To characterize the TID structures using these data, LoS TEC measurements for each satellite-receiver pair were detrended by first projecting the LoS TEC to vertical TEC (vTEC) using the thin shell approximation at 350-km altitude and subtracting the sliding 60-minute average. More details on this method can be found in Themens et al. (2022). The TEC anomalies are then binned in 0.75-degree latitude and longitude bins for mapping.

The Goddard Space Flight Center Space Physics Data Facility (<https://spdf.gsfc.nasa.gov/index.html>) and the National Space Science Data Center OMNIWeb (<http://omniweb.gsfc.nasa.gov>) (King and Papitashvili, 2005) archive the solar wind data. The magnetic field measurements obtained by Advanced Composition Explorer (ACE) (Smith *et al.*, 1998) are used.

### 3. AGWs/TIDs originating from lower thermosphere at high latitudes

van de Kamp et al. (2014) described two techniques to detect TIDs, one using the EISCAT incoherent scatter radar near Tromsø, and the other using the detrended GPS TEC data. They determined parameters characterizing TIDs and studied an event of January 20, 2010. While these authors did not investigate the origin of the TIDs they suggested that the AGWs were most likely generated at low atmospheric layers. Using the EISCAT Svalbard radars on February 13, 2001, Cai et al. (2011) observed moderately large-scale TIDs propagating over the dayside polar cap that were generated by the nightside auroral heating. It is noted that both these TID events occurred on days following arrivals of corotating interaction regions (CIRs) at the leading edge of solar wind high-speed streams that can trigger moderate geomagnetic storms (Tsurutani et al., 1990, 2006).

Frissell et al. (2016) concluded that polar atmospheric processes, namely the polar vortex, rather than space weather activity are primarily responsible for controlling the occurrence of high-latitude and midlatitude winter daytime medium-scale TIDs (MSTIDs). This paper has been frequently cited to justify suggestions of polar vortex as a source of the observed MSTIDs, particularly when geomagnetic activity is low. Recent papers referenced in Introduction (Becker et al., 2022; Bossert et al., 2022; Vadas et al., 2023) discussed methods for assessing vortex generated GWs from model

**Formatted:** Font: (Default) Times New Roman, (Asian) Times New Roman, 12 pt

**Formatted:** Font: (Default) Times New Roman, (Asian) Times New Roman, 12 pt

output. Vadas et al. (2023) discussed observations of polar vortex generated GWs and subsequent secondary GW generation in the polar region. Bossert et al. (2022) discussed a strong TID/TAD event observed during a sudden stratospheric warming (SSW) on January 18-19, 2013, and suggested that the large-scale TIDs/TADs were related to geomagnetic activity despite low  $Kp$  index. Thus, it is important to continue discussing possible sources of GWs from the lower and upper atmosphere.

(Bossert et al., 2021; Becker et al., 2022; Goncharenko et al., 2022). Bossert et al. (2021) studied gravity waves generated by stratospheric vortex on January 8, 2013, which they suggested had caused TIDs observed by PFISR in Poker Flat, Alaska. In Section 3.1, we examine this one case when PFISR in Poker Flat, Alaska. Observed TIDs during geomagnetically quiet period on January 8, 2013 event in the context of solar wind coupling to show evidence that the observed TIDs originated in the high-latitude dayside ionosphere poleward of Alaska.

In Section 3.2, we present observations of TIDs generated by solar wind-M-I-T coupling on the dayside, following the arrival of high-speed streams (HSSs) permeated by solar wind Alfvén waves (Belcher and Davis, 1971; Tsurutani et al., 1987). Solar wind Alfvén waves can modulate ionospheric convection and currents producing polar cap density patches and TIDs (Prikryl et al., 1999, 2005, 2022). Solar wind high-speed streams (HSSs) are associated with high-intensity, long-duration continuous auroral electrojet activity (HILDCAAs) that includes auroral substorms (Tsurutani and Gonzalez, 1987; Tsurutani et al., 1990, 1995). HILDCAAs are caused by trains of solar wind Alfvén waves (Belcher and Davis, 1971) that couple to the magnetosphere-ionosphere system (Dungey, 1961, 1995). This coupling extends to the neutral atmosphere and ionosphere because it is a source of aurorally excited gravity waves. Solar wind modulation of cusp particle signatures was associated with ionospheric flows (Rae et al., 2004). Solar wind Alfvén waves can modulate ionospheric convection and currents, most directly on the dayside, producing polar cap density patches and AGW/TIDs (Prikryl et al., 1999, 2005, 2022). The mechanisms for energy transfer to the thermosphere can be Joule heating, precipitation, or ion drag by Lorentz force (Chimonas and Hines, 1970; Chimonas, 1970; Testud, 1970; Richmond, 1978). On the dayside, it could be Joule heating, or the ion drag by swings in convection (PIFs) generating AGWs, which

**Formatted:** Font: (Default) Times New Roman, (Asian) Times New Roman, 12 pt

**Formatted:** Font: (Default) Times New Roman, (Asian) Times New Roman, 12 pt, Italic

**Formatted:** Font: (Default) Times New Roman, (Asian) Times New Roman, 12 pt

**Formatted:** Font: (Default) Times New Roman, (Asian) Times New Roman

**Formatted:** Font: (Default) Times New Roman, (Asian) Times New Roman

**Formatted:** Font: (Default) Times New Roman, (Asian) Times New Roman

**Formatted:** Font: (Default) Times New Roman, (Asian) Times New Roman

**Formatted:** Font: (Default) Times New Roman, (Asian) Times New Roman

**Formatted:** Font: Not Italic

**Formatted:** Font: (Default) Times New Roman, (Asian) Times New Roman, 12 pt, Not Italic

**Formatted:** Font: (Default) Times New Roman, (Asian) Times New Roman, 12 pt

**Formatted:** Font: (Default) Times New Roman, (Asian) Times New Roman, 12 pt, Not Italic

**Formatted:** Font: (Default) Times New Roman, (Asian) Times New Roman, 12 pt, Not Italic

in turn modulate ionospheric densities resulting in TIDs that are observed by SuperDARN radars (Samson et al., 1989; 1990).

### 3.1. Event of January 8/9, 2013

In the period from January 8 to 15 the PFISR beams scanned electron densities,  $N_e$  ( $\text{cm}^{-3}$ ), at altitudes from 150 to 500 km. In the detrended TEC maps over Alaska (<https://aer-nc-web.nict.go.jp/GPS/GLOBAL/MAP/2013/008/index.html>) the equatorward propagating TIDs were observed on each day during the daytime hours when the PFISR density data show signatures of downward propagating phase of TIDs. Fig. 1a shows  $N_e$  in logarithmic scale as a function of altitude observed by the radar beam 2 at temporal resolution of 3 min between 18:00 and 03:00 UT (09:00 and 18:00 LT) on January 8-9, 2013. The downward propagating phase of TIDs is readily seen superposed on the background of high daytime densities. To remove the background and highlight the TIDs with periods  $> 40$  min the time series for each altitude are detrended using a 33-point wide Savitzky-Golay filter (4<sup>th</sup> degree, 2<sup>nd</sup> order) (Fig. 1b). To show the equatorward propagation of the TIDs across Alaska, Fig. 1c shows the detrended GNSS vTEC mapped at latitude bins along the longitude of the PFISR.

~~Bossert et al. (2021) argued that because this event occurred during a geomagnetically quiet period, other than auroral sources should be considered for the observed TIDs, namely, the polar vortex.~~

The geomagnetic activity on January 8 was low, with the  $Kp$ -index  $\leq 1$  except for a peak of 3- in the last 3-hourly interval caused by a substorm that occurred in the European sector. The northernmost magnetometer in Alaska in Barrow observed the north-south  $X$ -component magnetic field perturbation of  $\sim 230$  nT at 17:10 UT (see Fig. S2 in the Supplement) indicating the westward electrojet. At this time, the IMF was pointing downward ( $B_y < 0$ ) and eastward flows (see Fig. S3a in the Supplement) in the dawn convection cell corresponded with the westward electrojet sensed in Barrow. After 18:00 UT, as the IMF  $B_y$  reversed to duskward (Figure 2c), the convection cells receded further poleward of Alaska and the convection pattern become dominated by the dusk cell (see Fig. S3b in the Supplement). At this time, the distant westward electrojet over Beaufort Sea could no longer be detected by magnetometers.

Formatted: Font: (Default) Times New Roman, (Asian) Times New Roman, 12 pt, Not Italic

Formatted: Font: (Default) Times New Roman, (Asian) Times New Roman, 12 pt, Not Italic

The King Salmon Radar (KSR) beam 9 pointing northwest over the East Siberian Sea observed positive (towards the radar) line-of-sight (LoS) velocities indicating quasiperiodic (20-50 min) pulsed ionospheric flows (PIFs; Fig. 2a) in the dawn convection cell. At near ranges, the KSR radar observed enhancements in the sea scatter power (Fig. 2b) caused by a series of equatorward propagating TIDs. The Prince George Radar (PGR) beam 1 also observed the TIDs in the ground scatter power (Fig. 2d). The periodicities of these TIDs were similar to those of PIFs and the TIDs observed by PFISR (Fig. 2c).

The IMF southward turnings are expected to result in enhanced reconnection rate leading to intensifications of the ionospheric convection/currents in the cusp footprint that were sources of TIDs. One of the convection enhancements can be viewed in Fig. S3b in the Supplement. The time series of the ACE IMF  $B_y$  and  $B_z$ , as well as the clock angle ( $B_z$ ,  $B_y$ ) counted from the geomagnetic north, with the  $180^\circ$  (dotted line) indicating southward turnings of the IMF are shown time-shifted in Fig. 2c. Normalized FFT spectra of the detrended IMF  $B_z$ ,  $B_y$ , and the Prince George radar ground scatter power (beam 1, gate 30, slant range 1530 km) are shown in the inset in Figure 2d. The spectra of the IMF  $B_z$  and the Prince George radar ground scatter power are very similar thus providing evidence that the generation of TIDs was driven by solar wind coupling to the dayside magnetosphere. The clock angle controls the reconnection rate at the magnetopause (Milan et al., 2012). The TIDs can be approximately associated with southward IMF turnings (positive deflections of the clock angle values towards  $180^\circ$  marked by arrows in Fig. 2). Of course, this is an approximate correspondence. The IMF observed by ACE does not represent exactly the IMF impacting the dayside magnetopause. It would require at least a spacecraft in front of the bow shock to monitor the IMF (e.g., Prikryl et al. 2002). But the observations of pulsed ionospheric flows and corresponding TIDs provide sufficient evidence that points to sources of these TIDs in the high-latitude ionosphere (Prikryl et al., 2022).

This assessment provides evidence that the observed TIDs could have originated from the magnetosphere/solar wind forcing rather than due to lower-atmospheric forcing. This highlights the significant challenge that exists in clearly identifying the source of TIDs in ionospheric observations and shows that a broad range of factors need to be considered together when attributing TID sources.

**Formatted:** Font: (Default) Times New Roman, (Asian)  
Times New Roman, 12 pt, Not Italic

**Formatted:** Font: (Default) Times New Roman, (Asian)  
Times New Roman, 12 pt, Not Italic

While we focused here on January 8/9, on each day during the PFISR experiment from January 8 to 15 the solar wind-MIT coupling that modulated PIFs in the ionospheric cusp footprint poleward of Alaska launched TIDs that were observed by PFISR, as well as in the GNSS vTEC maps. Similarly, in the European sector, dayside TIDs propagating equatorward from their sources in the cusp over Svalbard were also observed. This can be viewed in Fig. S4 in the Supplement.

### 3.2. Events of November 1 and 4-5, 2014

Solar wind Alfvén waves permeate HSSs, and along with CIRs, are highly geoeffective when IMF  $B_z < 0$  (Tsurutani et al., 1987, 1995, 2006). Following arrivals of HSS/CIRs (marked by asterisks in Fig. 3) on November 1 and 5, 2014, the solar wind Alfvén waves are characterized by the Walén relation between velocity  $V$  and magnetic field  $B$  (Yang, Chao and Lee, 2020). The components of the corresponding components of the magnetic field ( $B_y$  and  $B_z$ ) and velocity ( $V_y$  and  $V_z$ ) observed by ACE are correlated (Fig. 4a), a signature of solar wind Alfvén waves.

In the European sector, the SuperDARN Hankasalmi radar observed PIFs in the cusp over Svalbard and equatorward propagating TIDs that were also observed in the detrended vTEC. Figs. 5 and 6 show the ionospheric LoS velocities and the radar scatter power (ground scatter shown in grey color in the velocity plot) observed by the radar beam 11 on November 1 and 5, respectively. The ground magnetic field perturbations of the X-component observed in Ny Ålesund (NAL; <https://space.fmi.fi/image/www/index.php>) and 1D equivalent currents estimates that use all IMAGE magnetometers are superposed. The radar observed a series of intensifications of the negative (away from the radar) LoS velocities (PIFs) at ranges greater than ~2000 km on the dayside, starting at ~07:00 UT with the onset of ionospheric currents fluctuations sensed by the NAL magnetometer. The solar wind Alfvén waves modulated the dayside ionospheric currents launching AGWs driving the equatorward propagating TIDs observed in the radar ground scatter at ranges below ~2000 km. For November 1 the first event, Figs. 4b and 4c show the FFT spectra of detrended time series of IMF  $B_z$ , solar velocity  $V_z$ , the NAL X-component, and the Hankasalmi radar ground scatter power displaying peaks at similar frequencies/periods. For November 5, the FFT spectra can be viewed in Figs. S54b and S54c in the Supplement. The radar ground scatter

Formatted: Justified, Line spacing: 1.5 lines

(Figs. 5b and 6b) at ranges between 1000 and 1800 km shows tilted bands due to equatorward propagating MSTIDs (wavelengths < 1000 km).

Figs. 7a and 7b show the TIDs observed in the detrended vTEC as alternating positive and negative anomalies mapped along longitude of 15°E on November 1 and 5, respectively. The equatorward TIDs were observed at least down to latitude of 50°N, where the equatorward motion appears to be disrupted due to interference with TIDs from tropospheric sources moving eastward to southeastward that are discussed in Section 4.

The arrival of the HSS/CIR on November 4 triggered a minor geomagnetic storm with the *Dst* index reaching maximum negative value of -44 nT (Fig. 3) (Gonzalez *et al.*, 1994). Similar to cases reported previously (Prikryl *et al.*, 2022), intense ionospheric currents in the North American sector auroral zone launched large-scale TIDs (LSTIDs; wavelengths of 1000 km or more) that were observed by the midlatitude SuperDARN radars and the detrended TEC. Before 4:00 UT at radar frequency at 11.5 MHz, the Fort Hays West (FWH) midlatitude radar beam 12 looking northwest over the central Canada observed the ionospheric scatter showing enhancements in the positive LoS velocities (toward the radar; Fig. 8a) due to fluctuating eastward ionospheric flows at the equatorward edge of an expanded dawn convection cell associated with the fluctuating westward electrojet. The ionospheric currents were sensed by magnetometers, including one in Fort Simpson (FSIM; [www.carisma.ca/](http://www.carisma.ca/)). The X component of the ground magnetic field and time series of the latitudinal maxima in EICs at the longitude of 120°W, are superposed. After 14:00 UT, when the radar frequency was set to 15 MHz, the HF propagation allowed to observe TIDs in the ground scatter. Instead of the slant range, to reflect the actual TID location in the ionosphere, the ground-scan range mapping (Bristow, Greenwald and Samson, 1994; Frissell *et al.*, 2014) can be applied. In this case, the slant ranges between 1000 and 3000 km correspond to the mapped ground scatter range between 200 and 1200 km.

Two major intensifications of the westward electrojet at ~13:10 and 14:10 UT launched LSTIDs observed in the ground scatter starting at ~14:00 and 15:00 UT (Fig. 8b). The mapped EICs in Fig. 9a show the first major intensification of the westward electrojet (the EIC maxima at each

longitude are highlighted). It launched an equatorward propagating LSTID observed in the detrended vTEC maps (Fig. 9b). The second intensification of the westward electrojet launched another LSTID observed in the radar ground scatter starting at ~15:00 UT (Fig. 8b), as well as in the detrended vTEC. Figs. 10a and 10b show the LSTIDs observed in the detrended vTEC mapped along longitude of 100°W and 15°E, respectively. In the North American sector, the LSTIDs were observed between 13:00 and 16:00 UT (Fig. 10a).

In Europe, ~~during the most disturbed time of (HSS/CIR arrival) on November 4 the dayside auroral oval expanded down to latitude ~63°N. Fig. 10b shows the equivalent ionospheric currents estimated from the IMAGE magnetometers. LSTIDs (Fig. 9c) that that were launched by intensifications of dayside the east electrojet ionospheric currents over Svalbard~~ were observed propagating equatorward to mid latitudes between 11:00 and 18:00 UT (Figs. 9c and 10b). ~~HD equivalent currents estimates that use all IMAGE magnetometers are~~

In summary, the cases discussed in Sections 3.1 and 3.2 highlight the importance of solar wind coupling to the M-I-T system, particularly on the dayside, in the generation of AGWs/TIDs. The fluctuations of the IMF, sometimes Alfvénic, modulate ~~PIFs and the~~ ionospheric currents in the cusp ~~launching driving GW/TIDs. Intensifications of auroral electrojets launch LSTIDs.~~

#### 4. AGWs/TIDs originating from sources in the troposphere

In this section we focus on MSTIDs in mid latitudes that originated from tropospheric weather systems and were observed by HF Doppler sounders as well as by the GNSS TEC mapping technique. At mid to low latitudes, ~~the animations of detrended TEC maps show that~~ the azimuth of MSTIDs varies ~~(see Video in the Supplement)~~, suggesting ~~possible convective~~ sources in the troposphere ~~(e.g., Azeem et al., 2018).~~

MSTIDs caused by GWs with periods of 10-40 min propagating obliquely upward in the thermosphere/ionosphere were studied using multi-frequency and multi-point continuous HF Doppler sounding system located in the western part of Czechia from July 2014 to June 2015 (Chum et al., 2021). The observed azimuths depend on season with southeastward propagation

more likely in winter months, suggesting that cold season low pressure systems in the northeast Atlantic are sources of the GWs, which supports previously published results referenced above and points to winter jet stream as a likely source of GWs. In this section we examine such cases and trace TIDs in detrended TEC maps propagating from sources over the east Atlantic eastward/southeastward, and over the HF Doppler sounders that observed the medium-scale GWs.

#### *4.1. Events of November 1-8, 2014*

The 2-D propagation analysis of the HF Doppler sounders data for several events was applied to selected time intervals that exclude data gaps and to select time intervals in which the phase shifts/time delays between signals corresponding to different sounding paths (transmitter-receiver pairs) were approximately constant. Spectral and propagation analysis for all available 7.04 MHz signals from November 1 to 8, 2014 was performed (Fig. 11). Only daytime values are available because the critical frequency foF2 is too low at night (most of the nights are also not available at 4.65 MHz). On November 6 an enhanced noise (electromagnetic interference) prevented reliable analysis for a substantial part of the day. Fig. 11b shows dynamic spectra (periodograms) of Doppler shift signal obtained as the average of the maxima of three power spectral densities corresponding to three different transmitter – receiver pairs (Section 2) shown in Fig. 11a (including artificial offsets). The observed periods (Fig. 11b) range from 10 to about 40 min. The propagation azimuths (Fig. 11c) were mostly from 100 to about 160° (waves propagating south-eastward). In all cases, the azimuth is only plotted if the averaged Doppler fluctuations exceeded 0.12 Hz, the estimate of uncertainty of azimuth is less than 10° and the estimate of uncertainty in velocity is less than 10%. The phase velocities fluctuated typically between 100 and 200 m/s. Fig. 12 shows the analysis results on an expanded time scale to better see the TID characteristics for November 8.

During the period from November 1 to 8, 2014, we distinguish between aurorally-generated TIDs propagating equatorward from high latitudes (Section 3.2) and south-eastward propagating MSTIDs at mid latitudes by observed origin location. The south-eastward propagating MSTIDs were observed by the HF sounders and detrended vTEC. Low-pressure systems deepening over the North-east Atlantic, shown in the surface pressure analysis charts ([https://www1.wetter3.de/archiv\\_ukmet\\_dt.html](https://www1.wetter3.de/archiv_ukmet_dt.html)), were likely sources of MSTIDs propagating

eastward to southeastward, as observed in the detrended vTEC maps (indicated by arrows in Figs. 13a,b) on November 1 and 8, 2014. At the same time, the vTEC maps on both days also reveal equatorward propagating TIDs at latitudes down to  $\sim 50^\circ\text{N}$  that originated in the cusp ionospheric footprint over Svalbard, as already discussed in Section 3.2.

The Doppler shift spectrograms (Fig. 14a) recorded at frequency 7.04 MHz on November 1 and 8, 2014 show temporal evolution of power spectral densities (color-coded arbitrary units) of received signals that correspond to three different transmitter-receiver pairs. There was enhanced noise due to the electromagnetic interference on 8 November from about 9:30 to 12:30 UT. The straight horizontal line in the upper signal trace in the spectrogram corresponds to ground wave from one of the transmitters, located only  $\sim 7$  km from the receiver. The middle and bottom signal traces in the spectrogram correspond to other two transmitters. As described in more detail by Chum and Podolská (2018) and Chum et al. (2021), the use of well correlated signals at two or three different frequencies makes it possible to determine a 3-D phase velocity vector. The results that are summarized in Table S1 in the Supplement separately for the observation at frequencies of 4.65 and 7.04 MHz show mostly similar values of horizontal velocities (ranging from  $\sim 100$  to  $200$  m/s) and azimuths (ranging from  $\sim 90$  to  $145^\circ$ ).

In Fig. 14b (middle panels), the detrended vTEC mapped along the latitude of  $50^\circ$  shows eastward propagating TIDs towards the longitude of the HF sounding system that observed the TIDs (top panels). The bottom panels (Fig. 14c) show time series of the detrended vTEC at longitude of  $7^\circ\text{E}$  and the normalized FFT spectra that show peaks at periodicities of MSTIDs similar to those in Figs. 11b and 12b.

Cases of MSTIDs associated with intense low pressure systems were also observed on November 3 ( $\sim 08:00$ - $13:00$  UT) (see Fig. S65 in the Supplement), November 7 ( $\sim 08:00$ - $13:00$  UT) (see Fig. S76 in the Supplement), November 22 ( $\sim 08:00$ - $09:00$  UT), November 24 ( $\sim 07:30$ - $10:30$  UT), December 9 ( $\sim 08:30$ - $09:50$  and  $12:00$ - $13:50$  UT), December 10 ( $\sim 07:30$ - $09:50$  and  $12:00$ - $13:30$  UT), and December 24 ( $\sim 10:00$ - $14:00$  UT).

In summary, the south-eastward propagating MSTIDs observed in the detrended vTEC maps and by the HF Doppler sounders likely originated from intense low-pressure systems in the North-east Atlantic.

#### 4.2. Physical mechanism of GW generation in the troposphere

While tropospheric convection is a common source of gravity waves, no deep convection could be identified in the cold fronts of low-pressure systems over the North-east Atlantic (<https://www.ncdc.noaa.gov/gibbs/html/MSG-3/IR/2014-11-01-0>). Mesoscale gravity waves generated by geostrophic adjustment processes and shear instability have been observed (Uccellini and Koch, 1987; Koch and Dorian, 1988). Plougonven and Zhang (2014) reviewed the current knowledge and understanding of gravity waves near jets and fronts. Plougonven and Teitelbaum (2003; their Figure 2) showed patterns of alternating bands of convergence and divergence in maps of divergence of the horizontal wind for the lower stratosphere, which have been interpreted as the signature of inertia-gravity waves propagating upwards above the tropopause. A conceptual model of a common synoptic pattern has been identified with a source of gravity waves near the axis of inflection in the 300-hPa geopotential height field (Koch and O’Handley, 1997; their Figure 2).

In Section 4.1, the cases of MSTIDs on November 1 and 8, 2014 (Figs. 13 and 14) propagating eastward to southeastward observed by the HF Doppler sounding system and in the detrended vTEC maps are attributed to sources in the troposphere, namely deepening low pressure weather systems. This is consistent with the conceptual model referenced above. Using the ERA5 reanalysis (Hersbach *et al.*, 2020), Fig. 15 shows the 300-hPa geopotential height, approximate axis of inflection (a probable source region of gravity waves that is indicated by red dashed line), and horizontal winds at 300 hPa on November 1 and 8, 2014. Fig. 15b shows the divergence of the horizontal wind at 150-hPa level. The alternating bands of convergence and divergence are similar to those interpreted by Plougonven and Teitelbaum (2003) as gravity waves propagating to the lower stratosphere. Other cases of MSTIDs on November 3 and 7 can be viewed in Figs. S65 and S76 in the Supplement.

~~As mentioned in Section 3, I~~ in the case of the TID event ~~over Alaska~~ on January 8/9, 2013 that we attributed to auroral sources poleward of Alaska (Section 3), ~~Bossert et al. (2021) observed GWs~~

~~generated by stratospheric vortex.~~ There was an extratropical cyclone intensifying just south-west of Alaska. Using the ERA5 reanalysis, similar to Figs. 15e,f, north-eastward propagating GWs in the stratosphere are found (Fig. S87 in the Supplement) but no corresponding TIDs can be resolved in the detrended TEC maps, possibly because of sparse coverage by GNSS receivers. However, mesoscale GWs propagating eastward and upward into the stratosphere generated by geostrophic adjustment processes and shear instability may be common and could be driving MSTIDs.

## 5. Discussion

The solar wind – MIT coupling is known to modulate the intensity of ionospheric currents, including the auroral electrojets, which in turn launch atmospheric gravity waves causing TIDs. The cases of dayside equatorward propagating TIDs were observed with PFISR, SuperDARN, and detected in the detrended GNSS vTEC maps. This is consistent with previously published results and interpretations (e.g., Prikryl et al. 2022; and references therein). The dayside TIDs are commonly generated in the ionospheric footprint of the cusp. They were observed every day over Alaska during the PFISR experiment (8-15 January 2013) and in Europe (1-8 November 2014).

In Section 3.1, we have shown evidence that even during a geomagnetically very quiet period the TIDs that were observed by PFISR in Alaska can be attributed to sources at high latitudes. Quasiperiodic intensifications of the high-latitude ionospheric convection that were the source of these TIDs were observed poleward of Alaska over the East Siberian and Beaufort Seas. The ionospheric currents associated with PIFs could not be detected by ground magnetometers, and the  $Kp$  index indicated a quiet period. The ionospheric footprint of the cusp where the pulsed ionospheric flows and associated currents are sources of TIDs may be located further poleward of any ground magnetometers.

Regarding TIDs originating from the troposphere, there has been plentiful evidence of neutral atmosphere-ionosphere coupling via atmospheric gravity waves propagating into the upper atmosphere from sources in the lower atmosphere including convective storms (Alexander, 1996). Azeem and Barlage (2018) and Vadas and Azeem (2021) presented cases of convective storm generating TIDs, which exhibited partial to full concentric, or almost plane-parallel phase fronts. The latter TIDs were generated by extended squall line (Azeem and Barlage, 2018). However, in

the cases discussed in Section 4.1 there was no significant convection in the cold fronts that would generate such TIDs. The eastward propagating MSTIDs observed in the detrended  $\nu$ TEC maps and by the HF originated from low pressure sounding system were likely driven by GWs generated by geostrophic adjustment processes and shear instability in the troposphere.

In this study we have attempted to trace the observed TIDs to sources of AGWs in the upper and lower atmosphere, and to identify physical mechanisms. The solar wind coupling to the M-I-T system can generate equatorward propagating TIDs even during geomagnetically quiet conditions. Intensifying low pressure weather systems can generate AGWs propagating to the lower stratosphere and beyond, driving TIDs even when there is no significant tropospheric convection. More work needs to be done to better understand such cases, and many aspects of the system as a whole should be considered when determining the source of TIDs, as simple metrics/indices hide critical details.

## 6. Summary and conclusions

Traveling ionospheric disturbances are observed by radars, Doppler sounders, and the GNSS TEC mapping technique. Medium- to large-scale TIDs propagating equatorward were generated by solar wind coupling to the dayside magnetosphere-ionosphere-thermosphere modulating ionospheric convection and currents, including auroral electrojets. TIDs that were observed over Alaska by the Poker Flat incoherent scatter radar and by two SuperDARN radars are attributed to gravity waves generated in the ionospheric cusp footprint poleward of Alaska even when geomagnetic activity was low. Major intensifications of the westward electrojet over the North American sector launched LSTIDs observed by a mid-latitude SuperDARN radar and in the detrended global TEC maps. In the European sector, the equatorward propagating TIDs are attributed to solar wind Alfvén waves coupling to the dayside magnetosphere modulating ionospheric convection and currents in the cusp footprint over Svalbard. The cases of eastward to southeastward propagating MSTIDs observed at mid latitudes in the detrended GNSS TEC maps and by the HF Doppler sounders in Czechia originated from low pressure systems. The likely cause of these TIDs were gravity waves propagating from the troposphere and lower stratosphere that were generated by geostrophic adjustment processes, which have rarely been linked to TIDs previously.

500  
 501 *Data availability.* The solar wind data are provided by the NSSDC OMNI  
 502 (<http://omniweb.gsfc.nasa.gov>; NASA, 2022). The ground-based magnetometer data are  
 503 archived at the website of the Canadian Array for Realtime Investigations of Magnetic Activity  
 504 (CARISMA) (<https://www.carisma.ca/>; University of Alberta, 2022), and the IMAGE website at  
 505 <https://space.fmi.fi/image/www/index.php?>. The PFISR data are available  
 506 at <https://data.amisr.com/database/61/cal/2014/11/>. SuperDARN data are available  
 507 at <https://www.frdr-dfdr.ca/repo/collection/superdarn> (FRDR, 2022). Line-of-Sight TEC data can  
 508 be acquired from the Madrigal database (<http://cedar.openmadrigal.org/>; CEDAR, 2022) and  
 509 CHAIN GNSS data are available at [http://chain.physics.unb.ca/chain/pages/data\\_download](http://chain.physics.unb.ca/chain/pages/data_download)  
 510 (CHAIN, 2022).

511 Equivalent Ionospheric Currents (EICs) derived by the Spherical Elementary Currents Systems  
 512 (SECS) technique are archived at <http://vmo.igpp.ucla.edu/data1/SECS/> (SECS, 2022)  
 513 and [https://cdaweb.gsfc.nasa.gov/pub/data/aaa\\_special-purpose-datasets/spherical-elementary-](https://cdaweb.gsfc.nasa.gov/pub/data/aaa_special-purpose-datasets/spherical-elementary-and-equivalent-ionospheric-currents-weygand/)  
 514 [and-equivalent-ionospheric-currents-weygand/](https://cdaweb.gsfc.nasa.gov/pub/data/aaa_special-purpose-datasets/spherical-elementary-and-equivalent-ionospheric-currents-weygand/); <https://doi.org/10.21978/P8D62B>, Weygand,  
 515 2009a; <https://doi.org/10.21978/P8PP8X>, Weygand, 2009b). The Czech HF Doppler shift  
 516 spectrograms can be found in the archive at <http://datacenter.ufa.cas.cz/>.

517 GNSS data for this study were provided by the following organizations: International GNSS  
 518 Service (IGS), UNAVCO (<https://www.unavco.org/data/gps-gnss/gps-gnss.html>), Dutch  
 519 Permanent GNSS Array (<http://gnss1.tudelft.nl/dpga/rinex>), Can-Net (<https://www.can-net.ca/>),  
 520 Scripps Orbit and Permanent Array Center (Garner, <http://garner.ucsd.edu/pub/>), French Institut  
 521 Geographique National, Geodetic Data Archiving Facility (GeoDAF,  
 522 <http://geodaf.mt.asi.it/index.html>), Crustal Dynamics Data Information System (CDDIS,  
 523 <https://cddis.nasa.gov/archive/gnss/data/daily/>), National Geodetic Survey  
 524 (<https://geodesy.noaa.gov/corsdata/>), Instituto Brasileiro de Geografia e Estatística  
 525 ([http://geofitp.ibge.gov.br/informacoes\\_sobre\\_posicionamento\\_geodesico/rbmc/dados/](http://geofitp.ibge.gov.br/informacoes_sobre_posicionamento_geodesico/rbmc/dados/)), Instituto  
 526 Tecnológico Agrario de Castilla y Leon (ITACyL, <ftp://ftp.itacyl.es/RINEX/>), TrigNet South  
 527 Africa (<ftp://ftp.trignet.co.za>), The Western Canada Deformation Array (WCDA,  
 528 <ftp://wcda.pgc.nrcan.gc.ca/pub/gpsdata/rinex>), Canadian High Arctic Ionospheric Network  
 529 (CHAIN, [http://chain.physics.unb.ca/chain/pages/data\\_download](http://chain.physics.unb.ca/chain/pages/data_download)), Pacific Northwest Geodetic

530 Array (PANGA, <http://www.geodesy.cwu.edu/pub/data/>), Centro di Ricerche Sismologiche,  
 531 Système d'Observation du Niveau des Eaux Littorales (SONEL, <ftp://ftp.sonel.org/gps/data>),  
 532 INGV - Rete Integrata Nazionale GPS (RING, <http://ring.gm.ingv.it/>), RENAG : REseau  
 533 NAtional GPS permanent (<http://rgp.ign.fr/DONNEES/diffusion/>), Australian Space Weather  
 534 Services (<https://downloads.sws.bom.gov.au/wdc/gnss/data/>), GeoNet New Zealand  
 535 (<https://www.geonet.org.nz/data/types/geodetic>), National Land Survey Finland (NLS,  
 536 <https://www.maanmittauslaitos.fi/en/maps-and-spatial-data/positioning-services/rinex-palvelu>),  
 537 SWEPOS Sweden (<https://swepos.lantmateriet.se/>), Norwegian Mapping Authority (Kartverket,  
 538 <https://ftp.statkart.no/>), Geoscience Australia ([http://www.ga.gov.au/scientific-](http://www.ga.gov.au/scientific-topics/positioning-navigation/geodesy/gnss-networks/data-and-site-logs)  
 539 [topics/positioning-navigation/geodesy/gnss-networks/data-and-site-logs](http://www.ga.gov.au/scientific-topics/positioning-navigation/geodesy/gnss-networks/data-and-site-logs)), Institute of  
 540 Geodynamics, National Observatory of Athens (<https://www.gein.noa.gr/services/GPSData/>), and  
 541 European Permanent GNSS Network (EUREF,  
 542 [https://www.epncb.oma.be/ networkdata/data\\_access/dailyandhourly/datacentres.php](https://www.epncb.oma.be/networkdata/data_access/dailyandhourly/datacentres.php)).

543 *Author contributions.* PP and RGG contributed to conception and design of the study. PP, DRT,  
 544 JC, SC, RGG, and JMW acquired the resources and contributed to methodology, software, specific  
 545 data analysis, visualization, and organized the databases. PP wrote the first draft of the manuscript.  
 546 All authors contributed to manuscript revision and approved the submitted version.

547 *Competing interests.* The authors declare that they have no conflict of interest.

548 *Acknowledgments.* Infrastructure funding for CHAIN was provided by the Canada Foundation for  
 549 Innovation and the New Brunswick Innovation Foundation. CHAIN operation is conducted in  
 550 collaboration with the Canadian Space Agency (CSA). We are grateful to the Australian Bureau  
 551 of Meteorology, Space Weather Services for the provision of GNSS data. CDDIS is one of the  
 552 Earth Observing System Data and Information System (EOSDIS) Distributed Active Archive  
 553 Centers (DAACs), part of the NASA Earth Science Data and Information System (ESDIS) project.  
 554 Datasets and related data products and services are provided by CDDIS, managed by the NASA  
 555 ESDIS project. This material is based on services provided by the GAGE Facility, operated by  
 556 UNAVCO, Inc., with support from the National Science Foundation and the National Aeronautics  
 557 and Space Administration under NSF Cooperative Agreement EAR-1724794. A. Contributions by  
 558 the ACE (Norman F. Nees at Bartol Research Institute, David J. McComas at SWRI), NASA's  
 559 SPDF/CDAWeb, and the NSSDC OMNIWeb are acknowledged. The PFISR was developed under  
 560 NSF cooperative agreement ATM-0121483, and the data collection and analysis were supported

under NSF cooperative agreement ATM-0608577. The authors acknowledge the use of SuperDARN data. SuperDARN is a collection of radars funded by the national scientific funding agencies of Australia, Canada, China, France, Italy, Japan, Norway, South Africa, United Kingdom, and the United States of America. The Fort Hays SuperDARN radars are maintained and operated by Virginia Tech under support by NSF grant AGS-1935110, The King Salmon and Prince George radars are operated under support of NSF grant AGS--2125323 from the Upper Atmospheric Facilities Program, and by the Canada Foundation for Innovation, Innovation Saskatchewan and the Canadian Space Agency, respectively. We thank the many different groups operating magnetometer arrays for providing data for this study, including the THEMIS UCLA magnetometer network (Ground-based Imager and Magnetometer Network for Auroral Studies). The AUTUMNX magnetometer network is funded through the Canadian Space Agency/Geospace Observatory (GO) Canada program, Athabasca University, Centre for Science/Faculty of Science and Technology. The Magnetometer Array for Cusp and Cleft Studies (MACCS) array is supported by the US National Science Foundation grant ATM-0827903 to Augsburg College. The Solar and Terrestrial Physics (STEP) magnetometer file storage is at the Department of Earth and Planetary Physics, University of Tokyo and maintained by Kanji Hayashi (hayashi@grl.s.u-tokyo.ac.jp). The McMAC Project is sponsored by the Magnetospheric Physics Program of National Science Foundation through grant AGS-0245139. The ground magnetic stations are operated by the Technical University of Denmark, National Space Institute (DTU Space). The IMAGE magnetometer stations are maintained by 10 institutes from Finland, Germany, Norway, Poland, Russia, Sweden, Denmark, and Iceland. The Canadian Space Science Data Portal is funded in part by the Canadian Space Agency contract numbers 9 F007-071429 and 9 F007-070993. The Canadian Magnetic Observatory Network (CANMON) is maintained and operated by the Geological Survey of Canada. David R. Themens's contribution to this work is supported in part through CSA grant no. 21SUSTCHAI and through the United Kingdom Natural Environment Research Council (NERC) EISCAT3D: Fine-scale structuring, scintillation, and electrodynamics (FINESSE) (NE/W003147/1) and DRivers and Impacts of Ionospheric Variability with EISCAT-3D (DRIIVE) (NE/W003368/1) projects. James M. Weygand acknowledges NASA grant: 80NSSC18K0570, 80NSSC18K1220, NASA contract: 80GSFC17C0018 (HPDE), NAS5-02099(THEMIS). Shibaji Chakraborty thanks the National Science Foundation for support under grant AGS-1935110.

**Formatted:** Font: (Asian) Times New Roman

**Formatted:** Font: (Default) Times New Roman, (Asian) Times New Roman, 12 pt

**Formatted:** Font: (Default) Times New Roman, (Asian) Times New Roman, 12 pt

**Formatted:** Font: (Asian) Times New Roman

**Formatted:** Font: (Default) Times New Roman, (Asian) Times New Roman, 12 pt

*Financial support.* David R. Themens's contribution to this work is supported in part through CSA grant no. 21SUSTCHAI and through the United Kingdom Natural Environment Research Council (NERC) EISCAT3D: Fine-scale structuring, scintillation, and electrodynamics (FINESSE) (NE/W003147/1) and DRivers and Impacts of Ionospheric Variability with EISCAT-3D (DRIIVE) (NE/W003368/1) projects. J. Chum was funded by T-FORS project by European Commission (number SEP 210818055) and by the Johannes Amos Comenius Programme (P JAC), project No. CZ.02.01.01/00/22\_008/0004605, Natural and anthropogenic georisks“. James M. Weygand is supported by the NASA grant: 80NSSC18K0570, 80NSSC18K1220, NASA contract: 80GSFC17C0018 (HPDE), NAS5-02099 (THEMIS). Shibaji Chakraborty is supported by the National Science Foundation under grant AGS-1935110.

## References

Alexander, M. J.: A simulated spectrum of convectively generated gravity waves: Propagation from the tropopause to the mesopause and effects on the middle atmosphere, *Journal of Geophysical Research: Atmospheres*, 101(D1), pp. 1571–1588. doi: <https://doi.org/10.1029/95JD02046>, 1996.

Azeem, I. et al.: Multisensor profiling of a concentric gravity wave event propagating from the troposphere to the ionosphere, *Geophysical Research Letters*, 42(19), pp. 7874–7880. doi: <https://doi.org/10.1002/2015GL065903>, 2015.

Azeem, I. and Barlage, M.: Atmosphere-ionosphere coupling from convectively generated gravity waves, *Advances in Space Research*, 61(7), pp. 1931–1941. doi: <https://doi.org/10.1016/j.asr.2017.09.029>, 2018.

Azeem, I.: Asymmetry of near-noncentric traveling ionospheric disturbances due to Doppler-shifted atmospheric gravity waves, *Frontiers in Astronomy and Space Sciences*, 8, <https://doi.org/10.3389/fspas.2021.690480>, 2021.

Balthazor, R. L. and J., R.: A study of atmospheric gravity waves and travelling ionospheric disturbances at equatorial latitudes, *Ann. Geophys.*, 15. Available at: <http://www.ann-geophys.net/15/1048/1997/>, 1997.

Becker, E., Goncharenko, L., Harvey, V. L., & Vadas, S. L.: Multi-step vertical coupling during the January 2017 sudden stratospheric warming, *Journal of Geophysical Research: Space Physics*, 127, e2022JA030866. <https://doi.org/10.1029/2022JA030866>, 2022.

Becker, E., Vadas, S. L., Goncharenko, L., and Harvey, V. L.: Multi-step vertical coupling from the troposphere to the thermosphere due to gravity waves, in *EGU General Assembly Conference Abstracts*, pp. EGU22-10900. doi: 10.5194/egusphere-egu22-10900, 2022.

Formatted: Font: (Asian) Times New Roman

Formatted: Font: (Asian) Times New Roman

Formatted: Font: (Asian) Times New Roman

Formatted: Font: (Default) Times New Roman, (Asian) Times New Roman, 12 pt

Formatted: Font: (Default) Times New Roman, (Asian) Times New Roman, 12 pt, Not Italic

Formatted: Font: (Default) Times New Roman, (Asian) Times New Roman, 12 pt

Formatted: Font: (Asian) Times New Roman

Becker, E., Vadas, S. L., Bossert, K., Harvey, V. L., Zülicke, C., & Hoffmann, L.: A High-resolution whole-atmosphere model with resolved gravity waves and specified large-scale dynamics in the troposphere and stratosphere. *Journal of Geophysical Research: Atmospheres*, **127**, e2021JD035018. <https://doi.org/10.1029/2021JD035018>, 2022.

Formatted: Line spacing: single

Belcher, J. W., and Davis, L., Jr.: Large-amplitude Alfvén waves in the interplanetary medium, *J. Geophys. Res.*, **76**, 3534–3563, 1971.

Formatted: Font: (Asian) Times New Roman, English (United Kingdom), Check spelling and grammar

Formatted: Font: (Asian) Times New Roman

Bertin, F., Testud, J., Kersley, L., and Rees, P. R.: The meteorological jet stream as a source of medium scale gravity waves in the thermosphere: an experimental study, *Journal of Atmospheric and Terrestrial Physics*, **40**(10), pp. 1161–1183. doi: [https://doi.org/10.1016/0021-9169\(78\)90067-3](https://doi.org/10.1016/0021-9169(78)90067-3), 1978.

Bertin, F., Testud, J. and Kersley, L.: Medium scale gravity waves in the ionospheric F-region and their possible origin in weather disturbances, *Planetary and Space Science*, **23**(3), pp. 493–507. doi: [https://doi.org/10.1016/0032-0633\(75\)90120-8](https://doi.org/10.1016/0032-0633(75)90120-8), 1975.

Bossert, K., Becker, E., Kumari, K., and Conde, M.: Observations of stratospheric vortex generated gravity waves and subsequent impacts on thermosphere/ionosphere variability and traveling ionospheric disturbance generation, in *AGU Fall Meeting Abstracts*, pp. SA11B-07, 2021.

Bossert, K., Vadas, S. L., Hoffmann, L., Becker, E., Harvey, V. L., & Bramberger, M.: Observations of stratospheric gravity waves over Europe on 12 January 2016: The role of the polar night jet. *Journal of Geophysical Research: Atmospheres*, **125**, e2020JD032893. <https://doi.org/10.1029/2020JD032893>, 2020.

Formatted: Line spacing: single, No widow/orphan control

Bossert, K., Paxton, L. J., Matsuo, T., Goncharenko, L., Kumari, K., & Conde, M.: Large-scale traveling atmospheric and ionospheric disturbances observed in GUVI with multi-instrument validations. *Geophysical Research Letters*, **49**, e2022GL099901. <https://doi.org/10.1029/2022GL099901>, 2022.

Formatted: Font: (Default) Open Sans, (Asian) Open Sans, 10.5 pt, Font color: Custom Color(RGB(28,29,30)), English (Canada), Check spelling and grammar

Formatted: Font: (Asian) Times New Roman

Bristow, W. A., Greenwald, R. A. and Samson, J. C.: Identification of high-latitude acoustic gravity wave sources using the Goose Bay HF Radar, *Journal of Geophysical Research: Space Physics*, **99**(A1), pp. 319–331. doi: <https://doi.org/10.1029/93JA01470>, 1994.

Cai, H. T., Yin, F., Ma, S. Y., and McCrea, I. W.: Observations of AGW/TID propagation across the polar cap: a case study, *Annales Geophysicae*, **29**(8), pp. 1355–1363. doi: 10.5194/angeo-29-1355-2011, 2011.

Chimonas, G.: The equatorial electrojet as a source of long period travelling ionospheric disturbances, *Planetary and Space Science*, **18**(4), pp. 583–589. doi: [https://doi.org/10.1016/0032-0633\(70\)90133-9](https://doi.org/10.1016/0032-0633(70)90133-9), 1970.

Chimonas, G. and Hines, C. O.: Atmospheric gravity waves launched by auroral currents,

- Planetary and Space Science, 18(4), pp. 565–582. doi: 10.1016/0032-0633(70)90132-7, 1970.
- Chum J., Podolská K.: 3D analysis of GW propagation in the ionosphere. *Geophysical Research Letters*, 45, 11,562–11,571, <https://doi.org/10.1029/2018GL079695>, 2018.
- Chum, J., Podolská, K., Rusz, J., Baše, J., and Tedoradze, N.: Statistical investigation of gravity wave characteristics in the ionosphere, *Earth, Planets and Space*, 73(1), p. 60. doi: 10.1186/s40623-021-01379-3, 2021.
- Crowley, G. and Williams, P. J. S.: Observations of the source and propagation of atmospheric gravity waves, *Nature*, 328(6127), pp. 231–233. doi: 10.1038/328231a0, 1988.
- Dungey, J. W.: Interplanetary Magnetic Field and the Auroral Zones. *Phys. Rev. Lett.* 6, 47–48. <https://doi.org/10.1103/PhysRevLett.6.47>, 1961.
- Dungey, J. W.: Origin of the concept of reconnection and its application to the magnetopause: A historical view, *Physics of the Magnetopause. Geophysical Monograph 90*, edited by P. Song, B.U.O. Sonnerup, and M.F. Thomsen, pp. 17–19, AGU, Washington, D.C., 1995.
- Frissell, N. A., Baker, J. B. H., Ruohoniemi, J. M., Gerrard, A. J., Miller, E. S., Marini, J. P., West, M. L., and Bristow, W. A.: Climatology of medium-scale traveling ionospheric disturbances observed by the midlatitude Blackstone SuperDARN radar, *Journal of Geophysical Research: Space Physics*, 119(9), pp. 7679–7697. doi: <https://doi.org/10.1002/2014JA019870>, 2014.
- Frissell, N. A., Baker, J. B. H., Ruohoniemi, J. M., Greenwald, R. A., Gerrard, A. J., Miller, E. S., and West, M. L.: Sources and characteristics of medium-scale traveling ionospheric disturbances observed by high-frequency radars in the North American sector, *Journal of Geophysical Research: Space Physics*, 121(4), pp. 3722–3739, <https://doi.org/10.1002/2015JA022168>, 2016.
- Goncharenko, L., Harvey, V. L., Cullens, C., Becker, E., Zhang, S.-R., and Coster, A.: Influence of stratospheric gravity waves on TID activity at middle latitudes, in *EGU General Assembly Conference Abstracts*, pp. EGU22-6823, doi: 10.5194/egusphere-egu22-6823, 2022.
- Gonzalez, W. D., Joselyn, J. A., Kamide, Y., Kroehl, H. W., Rostoker, G., Tsurutani, B. T., and Vasyliunas, V. M.: What is a geomagnetic storm?, *Journal of Geophysical Research: Space Physics*, 99(A4), pp. 5771–5792, doi: <https://doi.org/10.1029/93JA02867>, 1994.
- Hajkowicz, L. A.: Auroral electrojet effect on the global occurrence pattern of large scale travelling ionospheric disturbances, *Planetary and Space Science*, 39(8), pp. 1189–1196., doi: [https://doi.org/10.1016/0032-0633\(91\)90170-F](https://doi.org/10.1016/0032-0633(91)90170-F), 1991.
- Heinselman, C. J. and Nicolls, M. J.: A Bayesian approach to electric field and E-region neutral wind estimation with the Poker Flat Advanced Modular Incoherent Scatter Radar, *Radio Science*, 43(5). doi: <https://doi.org/10.1029/2007RS003805>, 2008.

Formatted: Font: (Asian) Times New Roman

Formatted: Font: (Asian) Times New Roman

- Hersbach, H., Bell, B., Berrisford, P., Hirahara, S., Horányi, A., Muñoz-Sabater, J., Nicolas, J., Peubey, C., Radu, R., Schepers, D., Simmons, A., Soci, C., Abdalla, S., Abellan, X., Balsamo, G., Bechtold, P., Biavati, G., Bidlot, J., Bonavita, M., De Chiara, G., Dahlgren, P., Dee, D., Diamantakis, M., Dragani, R., Flemming, J., Forbes, R., Fuentes, M., Geer, A., Haimberger, L., Healy, S., Hogan, R. J., Hólm, E., Janisková, M., Keeley, S., Laloyaux, P., Lopez, P., Lupu, C., Radnoti, G., de Rosnay, P., Rozum, I., Vamborg, F., Villaume, S., and Thépaut, J.-N.: The ERA5 global reanalysis, *Q. J. R. Met. Soc.*, 146(730), pp. 1999–2049. doi: <https://doi.org/10.1002/qj.3803>, 2020.
- Hines, C. O.: Internal Atmospheric Gravity Waves At Ionospheric Heights, *Canadian Journal of Physics*, 38(11), pp. 1441–1481. doi: 10.1139/p60-150, 1960.
- Hocke, K. and Schlegel, K.: A review of atmospheric gravity waves and travelling ionospheric disturbances: 1982-1995, *Annales Geophysicae*, 14(9), pp. 917–940, doi: 10.1007/s00585-996-0917-6, 1996.
- Huang, C.-S., Sofko, G. J., Kustov, A. V., MacDougall, J. W., Andre, D. A., Hughes, W. J., and Papitashvili, V. O.: Quasi-periodic ionospheric disturbances with a 40-min period during prolonged northward interplanetary magnetic field, *Geophysical Research Letters*, 27(12), pp. 1795–1798, doi: <https://doi.org/10.1029/1999GL003731>, 2000.
- Huang, C.-S., Andre, D. A. and Sofko, G. J.: Observations of solar wind directly driven auroral electrojets and gravity waves, *Journal of Geophysical Research: Space Physics*, 103(A10), pp. 23347–23356. doi: <https://doi.org/10.1029/98JA02297>, 1998.
- Hunsucker, R. D.: Atmospheric gravity waves generated in the high-latitude ionosphere: A review, *Reviews of Geophysics*, 20(2), pp. 293–315, doi: 10.1029/RG020i002p00293, 1982.
- van de Kamp, M., Pokhotelov, D. and Kauristie, K.: TID characterised using joint effort of incoherent scatter radar and GPS, *Annales Geophysicae*, 32(12), pp. 1511–1532, doi: 10.5194/angeo-32-1511-2014, 2014.
- Kelley, I. J., Kunduri, B. S. R., Baker, J. B. H., Ruohoniemi, J. M., and Shepherd, S. G.: Storm Time Electrified MSTIDs Observed Over Mid-Latitude North America, *Journal of Geophysical Research: Space Physics*, 128(3), p. e2022JA031115, doi: <https://doi.org/10.1029/2022JA031115>, 2023.
- Kikuchi, T., Hashimoto, K.K.: Transmission of the electric fields to the low latitude ionosphere in the magnetosphere-ionosphere current circuit, *Geosci. Lett.* 3, 4, doi: <https://doi.org/10.1186/s40562-016-0035-6>, 2014.
- King, J. H. and Papitashvili, N.: Solar wind spatial scales in and comparisons of hourly Wind and ACE plasma and magnetic field data, *Journal of Geophysical Research*, 110(A2), p. A02104. doi: 10.1029/2004JA010649, 2005.
- Klostermeyer, J.: Lamb waves originating in nongeostrophic disturbances: A case study, *J. Geophys. Res.*, 82(9), 1441–1448, doi: [10.1029/JC082i009p01441](https://doi.org/10.1029/JC082i009p01441), 1977.

Formatted: Font: (Asian) Times New Roman

Formatted: Font: (Asian) Times New Roman

Koch, S. E. and Dorian, P. B.: A Mesoscale Gravity Wave Event Observed during CCOPE. Part III: Wave Environment and Probable Source Mechanisms, *Monthly Weather Review*, 116(12), pp. 2570–2592. doi: [https://doi.org/10.1175/1520-0493\(1988\)116<2570:AMGWEO>2.0.CO;2](https://doi.org/10.1175/1520-0493(1988)116<2570:AMGWEO>2.0.CO;2), 1988.

Koch, S. E. and OHandley, C.: Operational Forecasting and Detection of Mesoscale Gravity Waves, *Weather and Forecasting*, 12(2), pp. 253–281, doi: [https://doi.org/10.1175/1520-0434\(1997\)012<0253:OFADOM>2.0.CO;2](https://doi.org/10.1175/1520-0434(1997)012<0253:OFADOM>2.0.CO;2), 1997.

Lewis, R. V, Williams, P. J. S., Millward, G. H., and Quegan, S.: The generation and propagation of atmospheric gravity waves from activity in the auroral electrojet, *Journal of Atmospheric and Terrestrial Physics*, 58(6), pp. 807–820, doi: [https://doi.org/10.1016/0021-9169\(95\)00075-5](https://doi.org/10.1016/0021-9169(95)00075-5), 1996.

Mayr, H. G., Harris, I., Varosi, F., and Herrero, F. A.: Global Excitation of Wave Phenomena in a Dissipative Multiconstituent Medium. 1. Transfer Function of the Earth's Thermosphere, *Journal of Geophysical Research*, 89(A12), pp. 10929–10959, doi: 10.1029/JA089iA12p10929, 1984a.

Mayr, H. G., Harris, I., Varosi, F., and Herrero, F. A.: Global Excitation of Wave Phenomena in a Dissipative Multiconstituent Medium - 2. Impulsive Perturbations in the Earth's Thermosphere, *Journal of Geophysical Research*, 89(A12), pp. 10961–10986. doi: 10.1029/JA089iA12p10961, 1984b.

Mayr, H. G., Talaat, E. R. and Wolven, B. C.: Global propagation of gravity waves generated with the whole atmosphere transfer function model, *Journal of Atmospheric and Solar-Terrestrial Physics*, 104, pp. 7–17, doi: 10.1016/j.jastp.2013.08.001, 2013.

McWilliams, K. A., Yeoman, T. K. and Provan, G.: A statistical survey of dayside pulsed ionospheric flows as seen by the CUTLASS Finland HF radar, *Annales Geophysicae*, 18(4), pp. 445–453, doi: 10.1007/s00585-000-0445-8, 2000.

Milan, S. E., Gosling, J. S., and Hubert, B.: Relationship between interplanetary parameters and the magnetopause reconnection rate quantified from observations of the expanding polar cap, *J. Geophys. Res.*, 117, A03226, doi: [10.1029/2011JA017082](https://doi.org/10.1029/2011JA017082), 2012.

Millward, G.: A resonance effect in AGWs created by periodic recurrent bursts in the auroral electric field, *Annales Geophysicae*, 12(1), pp. 94–94, 1994.

Millward, G. H., Quegan, S., Moffett, R. J., Fuller-Rowell, T. J., and Rees, D.: A modelling study of the coupled ionospheric and thermospheric response to an enhanced high-latitude electric field event, *Planetary and Space Science*, 41(1), pp. 45–56, doi: 10.1016/0032-0633(93)90016-U, 1993a.

Millward, G. H., Moffett, R. J., Quegan, S., and Fuller-Rowell, T. J.: Effects of an atmospheric gravity wave on the midlatitude ionospheric F layer, *Journal of Geophysical Research: Space Physics*, 98(A11), pp. 19173–19179. doi: 10.1029/93ja02093, 1993b.

Formatted: Font: (Asian) Times New Roman

Formatted: Font: (Asian) Times New Roman

- Mrak, S., Semeter, J., Nishimura, Y., Hirsch, M., and Sivadas, N.: Coincidental TID Production by Tropospheric Weather During the August 2017 Total Solar Eclipse, *Geophysical Research Letters*, 45(20), pp. 10,903–910,911, doi: <https://doi.org/10.1029/2018GL080239>, 2018.
- Munteanu, C., Hamada, A., and Mursula, K.: High-speed solar wind streams in 2007–2008: Turning on the Russell-McPherron effect, *Journal of Geophysical Research: Space Physics*, 124, <https://doi.org/10.1029/2019JA026846>, 2019.
- Negrea, C., Munteanu, C., and Echim, M. M.: Global ionospheric response to a periodic sequence of HSS/CIR events during the 2007–2008 solar minimum, *Journal of Geophysical Research: Space Physics*, 126, e2020JA029071, <https://doi.org/10.1029/2020JA029071>, 2021.
- Nicolls, M. J., and Heinselman, C. J.: Three-dimensional measurements of traveling ionospheric disturbances with the Poker Flat Incoherent Scatter Radar, *Geophys. Res. Lett.*, 34, L21104, doi: [10.1029/2007GL031506](https://doi.org/10.1029/2007GL031506), 2007.
- Nishioka, M., Tsugawa, T., Kubota, M., and Ishii, M.: Concentric waves and short-period oscillations observed in the ionosphere after the 2013 Moore EF5 tornado, *Geophysical Research Letters*, 40(21), pp. 5581–5586, doi: <https://doi.org/10.1002/2013GL057963>, 2013.
- Nishitani, N., Ruohoniemi, J. M., Lester, M., Baker, J. B. H., Koustov, A. V., Shepherd, S. G., Chisham, G., Hori, T., Thomas, E. G., Makarevich, R. A., Marchaudon, A., Ponomarenko, P., Wild, J. A., Milan, S. E., Bristow, W. A., Devlin, J., Miller, E., Greenwald, R. A., Ogawa, T., and Kikuchi, T.: Review of the accomplishments of mid-latitude Super Dual Auroral Radar Network (SuperDARN) HF radars, *Progress in Earth and Planetary Science*, 6(1), p. 27, doi: [10.1186/s40645-019-0270-5](https://doi.org/10.1186/s40645-019-0270-5), 2019.
- Oliver, W. L., Otsuka, Y., Sato, M., Takami, T., and Fukao, S.: A climatology of F region gravity wave propagation over the middle and upper atmosphere radar, *Journal of Geophysical Research: Space Physics*, 102(A7), pp. 14499–14512, doi: <https://doi.org/10.1029/97JA00491>, 1997.
- Plougonven, R. and Teitelbaum, H.: Comparison of a large-scale inertia-gravity wave as seen in the ECMWF analyses and from radiosondes, *Geophysical Research Letters*, 30(18), doi: <https://doi.org/10.1029/2003GL017716>, 2003.
- Plougonven, R. and Zhang, F.: Internal gravity waves from atmospheric jets and fronts, *Reviews of Geophysics*, 52(1), pp. 33–76, doi: <https://doi.org/10.1002/2012RG000419>, 2014.
- Press, W. H. and Teukolsky, S. A.: Savitzky-Golay Smoothing Filters, *Comput. Phys.* 4 (6): 669–672, <https://doi.org/10.1063/1.4822961>, 1990.
- Prikryl, P., MacDougall, J. W., Grant, I. F., Steele, D. P., Sofko, G. J., and Greenwald, R. A.: Polar patches generated by solar wind Alfvén wave coupling to the dayside magnetosphere, *Advances in Space Research*, 23(10), doi: [10.1016/S0273-1177\(99\)00390-7](https://doi.org/10.1016/S0273-1177(99)00390-7), 1999.
- Prikryl, P., Provan, G., McWilliams, K. A., and Yeoman, T. K.: Ionospheric cusp flows pulsed by solar wind Alfvén waves, *Annales Geophysicae*, 20(2), doi: [10.5194/angeo-20-161-2002](https://doi.org/10.5194/angeo-20-161-2002),

Formatted: Font: (Asian) Times New Roman

Formatted: Font: (Asian) Times New Roman

Formatted: Font: (Asian) Times New Roman

Formatted: Font: (Asian) Times New Roman

Formatted: Font: (Asian) Times New Roman

Formatted: Font: (Asian) Times New Roman

815 2002.

816 Prikryl, P., Muldrew, D. B., Sofko, G. J., and Ruohoniemi, J. M.: Solar wind Alfvén waves: A  
817 source of pulsed ionospheric convection and atmospheric gravity waves, *Annales Geophysicae*,  
818 23(2), pp. 401–417, doi: 10.5194/angeo-23-401-2005, 2005.

819 Prikryl, P., Gillies, R. G., Themens, D. R., Weygand, J. M., Thomas, E. G., and Chakraborty, S.:  
820 Multi-instrument observations of polar cap patches and traveling ionospheric disturbances  
821 generated by solar wind Alfvén waves coupling to the dayside magnetosphere, *Annales*  
822 *Geophysicae*, 40(6), pp. 619–639, doi: 10.5194/angeo-40-619-2022, 2022.

823 Rae, I. J., Fenrich, F. R., Lester, M., McWilliams, K. A., and Scudder, J. D.: Solar wind  
824 modulation of cusp particle signatures and their associated ionospheric flows, *J. Geophys. Res.*,  
825 109, A03223, doi:10.1029/2003JA010188, 2004.

826 Richmond, A. D.: Gravity wave generation, propagation, and dissipation in the thermosphere,  
827 *Journal of Geophysical Research*, 83(A9), p. 4131, doi: 10.1029/ja083ia09p04131, 1978.

828 Samson, J. C., Greenwald, R. A., Ruohoniemi, J. M., and Baker, K. B.: High-frequency radar  
829 observations of atmospheric gravity waves in the high latitude ionosphere, *Geophysical Research*  
830 *Letters* 16, 875–878, 1989.

831 Samson, J. C., Greenwald, R. A., Ruohoniemi, J. M., Frey, A., Baker, K. B.: Goose bay radar  
832 observations of earth-reflected, atmospheric gravity-waves in the high-latitude ionosphere, *J.*  
833 *Geophys. Res.* 95(A6):7693–7709, <https://doi.org/10.1029/JA095iA06p07693>, 1990.

834 Smith, C. W., LHeureux, J., Ness, N. F., Acuña, M. H., Burlaga, L. F., and Scheifele, J.: The  
835 ACE Magnetic Fields Experiment, *Space Science Reviews*, 86(1), pp. 613–632. doi:  
836 10.1023/A:1005092216668, 1998.

837 Testud, J.: Gravity waves generated during magnetic substorms, *Journal of Atmospheric and*  
838 *Terrestrial Physics*, 32(11), pp. 1793–1805, doi: 10.1016/0021-9169(70)90137-6, 1970.

839 Themens, D. R., Jayachandran, P. T., Langley, R. B., MacDougall, J. W., and Nicolls, M. J.:  
840 Determining receiver biases in GPS-derived total electron content in the auroral oval and polar  
841 cap region using ionosonde measurements, *GPS Solutions*, 17(3), pp. 357–369. doi:  
842 10.1007/s10291-012-0284-6, 2013.

843 Themens, D. R., Watson, C., Žagar, N., Vasylyevych, S., Elvidge, S., McCaffrey, A., Prikryl, P.,  
844 Reid, B., Wood, A., and Jayachandran, P. T.: Global Propagation of Ionospheric Disturbances  
845 Associated With the 2022 Tonga Volcanic Eruption, *Geophysical Research Letters*, 49(7), p.  
846 e2022GL098158, doi: <https://doi.org/10.1029/2022GL098158>, 2022.

847 Themens, D. R., Jayachandran, P. T. and Langley, R. B.: The nature of GPS differential receiver  
848 bias variability: An examination in the polar cap region, *Journal of Geophysical Research: Space*  
849 *Physics*, 120(9), pp. 8155–8175, doi: <https://doi.org/10.1002/2015JA021639>, 2015.

Formatted: Font: 12 pt

Formatted: Font: (Default) Times New Roman, (Asian)  
Times New Roman, 12 pt

Formatted: Font: (Default) Times New Roman, (Asian)  
Times New Roman, 12 pt

Formatted: Font: (Default) Times New Roman, (Asian)  
Times New Roman, 12 pt

Formatted: Font: (Default) Times New Roman, (Asian)  
Times New Roman, 12 pt

Formatted: Font: (Default) Times New Roman, (Asian)  
Times New Roman, 12 pt

Formatted: Font: (Default) Times New Roman, (Asian)  
Times New Roman, 12 pt

Formatted: Font: (Asian) Times New Roman

Formatted: Font: (Default) Times New Roman, (Asian)  
Times New Roman

Formatted: Font: (Default) Times New Roman, (Asian)  
Times New Roman

Formatted: Font: (Default) Times New Roman, (Asian)  
Times New Roman

Formatted: Font: (Default) Times New Roman, (Asian)  
Times New Roman, Not Italic

Formatted: Font: (Default) Times New Roman, (Asian)  
Times New Roman

Formatted: Font: (Asian) Times New Roman

Formatted: Font: (Asian) Times New Roman

Formatted: Font: (Asian) Times New Roman

- 850 Tsurutani, B. T., and Gonzalez, W. D.: 1987 The cause of high-intensity long-duration  
 851 continuous AE activity (HILDCAAs): Interplanetary Alfvén wave trains, *Planet. Space*  
 852 *Sci.*, 35(4), 405–412, doi:10.1016/0032-0633(87)90097-3, 1987
- 853 Tsurutani, B. T., Gould, T., Goldstein, B. E., Gonzalez, W. D., and Sugiura, M.: Interplanetary  
 854 Alfvén waves and auroral (substorm) activity: Imp 8, *J. Geophys. Res.*, 95(A3), 2241–2252,  
 855 doi:10.1029/ja095ia03p02241, 1990.
- 856 Tsurutani, B. T., Gonzalez, W. D., Gonzalez, A. L. C., Tang, F., Arballo, J. K., and Okada, M.:  
 857 Interplanetary origin of geomagnetic activity in the declining phase of the solar cycle, *J.*  
 858 *Geophys. Res. Space Phys.*, 100(A11), 21717–21733, doi:10.1029/95ja01476, 1995.
- 859 Tsurutani, B. T., et al.: Corotating solar wind streams and recurrent geomagnetic activity: A  
 860 review, *J. Geophys. Res.*, 111, A07S01, doi:[10.1029/2005JA011273](https://doi.org/10.1029/2005JA011273), 2006.
- 861 Uccellini, L. W. and Koch, S. E.: The Synoptic Setting and Possible Energy Sources for  
 862 Mesoscale Wave Disturbances, *Monthly Weather Review*, 115(3), pp. 721–729, doi:  
 863 [https://doi.org/10.1175/1520-0493\(1987\)115<0721:TSSAPE>2.0.CO;2](https://doi.org/10.1175/1520-0493(1987)115<0721:TSSAPE>2.0.CO;2), 1987.
- 864 Vadas, S. L. and Nicolls, M. J.: Using PFISR measurements and gravity wave dissipative  
 865 theory to determine the neutral thermospheric winds, *Geophys. Res. Lett.*, 35, L02105,  
 866 doi:[10.1029/2007GL031522](https://doi.org/10.1029/2007GL031522), 2008.
- 867 Vadas, S. L. and Azeem, I.: Concentric secondary gravity waves in the thermosphere and  
 868 ionosphere over the continental United States on March 25–26, 2015 from deep Convection.  
 869 *Journal of Geophysical Research: Space Physics*, 126, e2020JA028275, [https://](https://doi.org/10.1029/2020JA028275)  
 870 doi.org/10.1029/2020JA028275
- 871 Vadas, S. L., Becker, E., Bossert, K., Baumgarten, G., Hoffmann, L., & Harvey, V. L.: Secondary  
 872 gravity waves from the stratospheric polar vortex over ALOMAR observatory on 12–14 January  
 873 2016: Observations and modeling. *Journal of Geophysical Research: Atmospheres*, 128,  
 874 e2022JD036985. <https://doi.org/10.1029/2022JD036985>, 2023.  
 875 ▲
- 876 Waldock, J. A. and Jones, T. B. (1987) Source regions of medium scale travelling ionospheric  
 877 disturbances observed at mid-latitudes, *Journal of Atmospheric and Terrestrial Physics*, 49(2),  
 878 pp. 105–114. doi: [https://doi.org/10.1016/0021-9169\(87\)90044-4](https://doi.org/10.1016/0021-9169(87)90044-4), 2021.
- 879 Williams, P. J. S., Viridi, T. S., Lewis, R. V., Lester, M., Rodger, A. S., McCrea, I. W., and  
 880 Freeman, K. S. C.: Worldwide atmospheric gravity-wave study in the European sector 1985–  
 881 1990, *Journal of Atmospheric and Terrestrial Physics*, 55(4–5), pp. 683–696, doi: 10.1016/0021-  
 882 9169(93)90014-P, 1993.
- 883 Yang, Y.-H., Chao, J.-K. and Lee, L.-C.: On the Walén Relation for Alfvénic Fluctuations in  
 884 Interplanetary Space, *The Astrophysical Journal*, 904(2), p. 195, doi: 10.3847/1538-4357/abfb55,  
 885 2020.
- 886 Yu, Y., Wang, W. and Hickey, M. P.: Ionospheric signatures of gravity waves produced by the

Formatted: Font: (Asian) Times New Roman

Formatted: Font: (Asian) Times New Roman

Formatted: Font: (Asian) Times New Roman

Formatted: Font: (Asian) Times New Roman

Formatted: Line spacing: single, No widow/orphan control

Formatted: Font: (Asian) Times New Roman, English (Canada), Check spelling and grammar

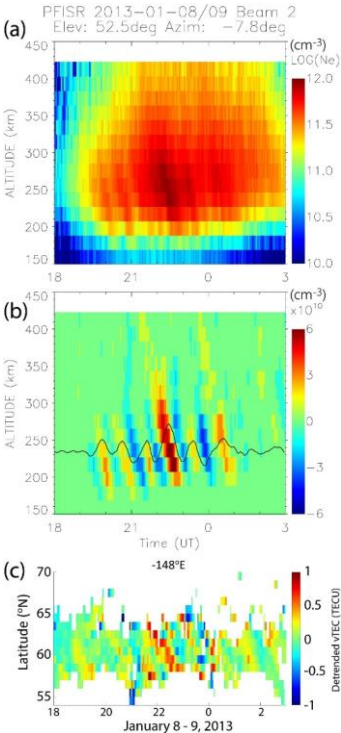
Formatted: Font: (Asian) Times New Roman

887 2004 Sumatra and 2011 Tohoku tsunamis: A modeling study, *Journal of Geophysical Research:*  
888 *Space Physics*, 122(1), pp. 1146–1162, doi: <https://doi.org/10.1002/2016JA023116>, 2017.

889 Zhang, S.-R., Erickson, P. J., Goncharenko, L. P., Coster, A. J., Rideout, W., and Vierinen, J.:  
890 Ionospheric Bow Waves and Perturbations Induced by the 21 August 2017 Solar Eclipse,  
891 *Geophysical Research Letters*, 44(24), pp. 12,12-67,73, doi:  
892 <https://doi.org/10.1002/2017GL076054>, 2017.

893 Zhang, S.-R., Coster, A. J., Erickson, P. J., Goncharenko, L. P., Rideout, W., & Vierinen, J.:  
894 Traveling ionospheric disturbances and ionospheric perturbations associated with solar flares in  
895 September 2017. *Journal of Geophysical Research: Space Physics*, 124, 5894–5917,  
896 <https://doi.org/10.1029/2019JA026585>, 2019,

897 **Figures**  
898



899 **Figure 1:** (a) Ionospheric density observed by the PFISR radar beam 2 and (b) detrended using a  
900 33-point wide Savitzky-Golay filter. (c) The detrended GNSS vTEC mapped at latitude bins  
901 along the longitude of PFISR.  
902

Formatted: Font: (Default) Times New Roman, (Asian) Times New Roman, 12 pt

Formatted: Font: (Default) Times New Roman, (Asian) Times New Roman, 12 pt

Formatted: Font: (Default) Times New Roman, (Asian) Times New Roman, 12 pt, Not Italic

Formatted: Font: (Default) Times New Roman, (Asian) Times New Roman, 12 pt

Formatted: Font: (Default) Times New Roman, (Asian) Times New Roman, 12 pt

Formatted: Font: (Default) Open Sans, (Asian) Open Sans, 10.5 pt

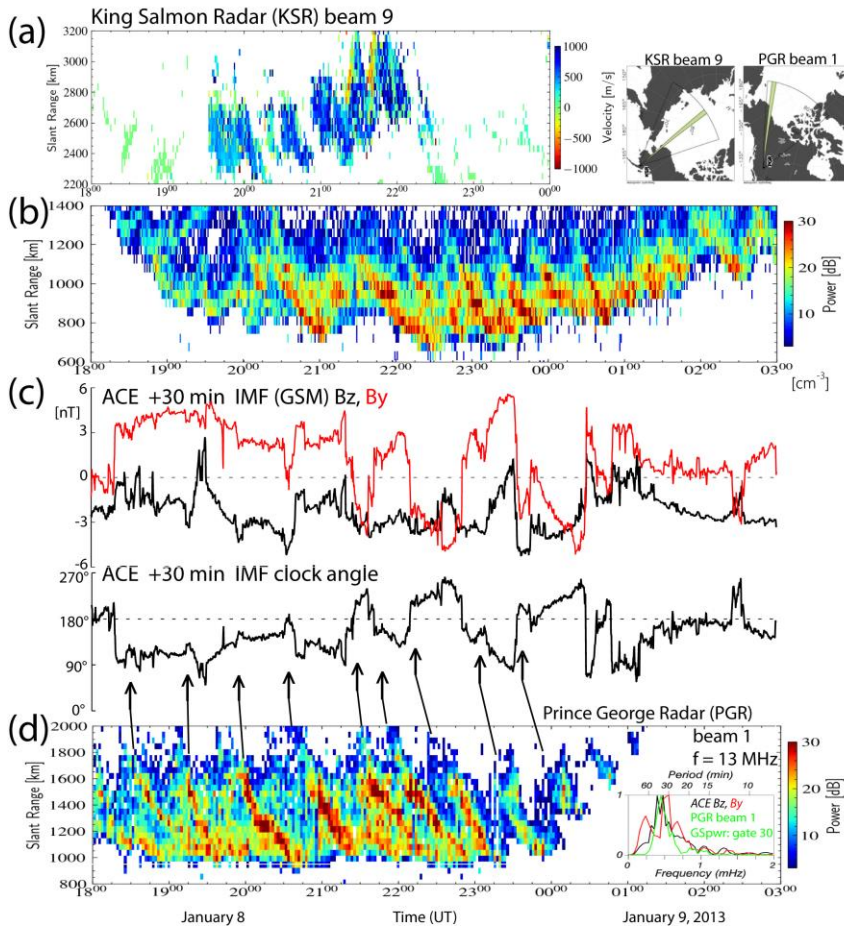


**Figure 2:** (a) The line-of-sight velocities and (b) the sea scatter power as a function of the slant range observed by the KSR radar beam 9. (c) Ionospheric density observed by the PFISR radar beam 2 detrended using a 15-point wide Savitzky-Golay filter. The time-shifted time series of the IMF  $B_z$ ,  $B_y$ , and the IMF clock angle observed by ACE spacecraft. (d) The ground scatter power observed by the PGR radar beam 1. The arrows indicate southward turning of the IMF. Normalized FFT spectra of the detrended IMF  $B_z$ ,  $B_y$ , and the Prince George radar ground scatter power (beam 1, gate 30, slant range 1530 km) are shown in the inset.

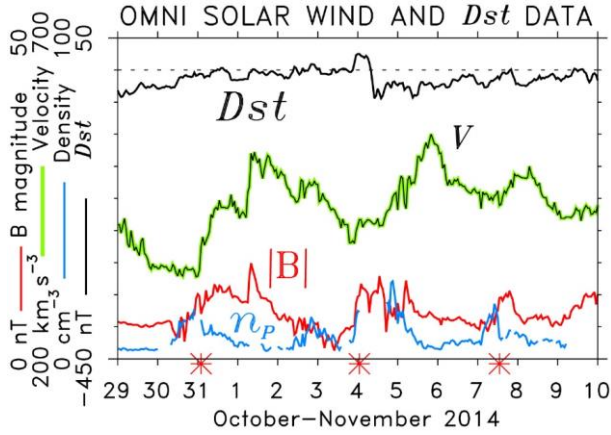


**Figure 3:** The OMNI solar wind velocity  $V$ , magnetic field magnitude  $|B|$ , and proton density  $n_p$  showing three HSS/CIRs on October 31, November 4 and 7 are marked by red asterisks at the time axis. The ring current  $Dst$  index is also shown.

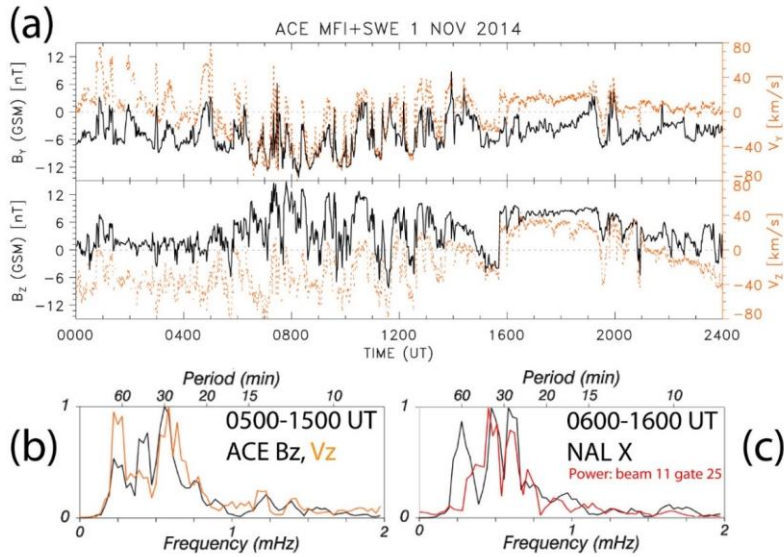


**Figure 4:** (a) The components of the magnetic field and solar wind velocity observed by ACE, (b) the FFT spectra of the detrended time series of IMF  $B_z$  and solar velocity  $V_z$ , and (c) the FFT spectra of the time series of the X-component of ground magnetic field perturbations in Ny Ålesund (NAL) and the Hankasalmi radar ground scatter power (beam 11, gate 25, slant range 1305 km; 06:50-16:50 UT).

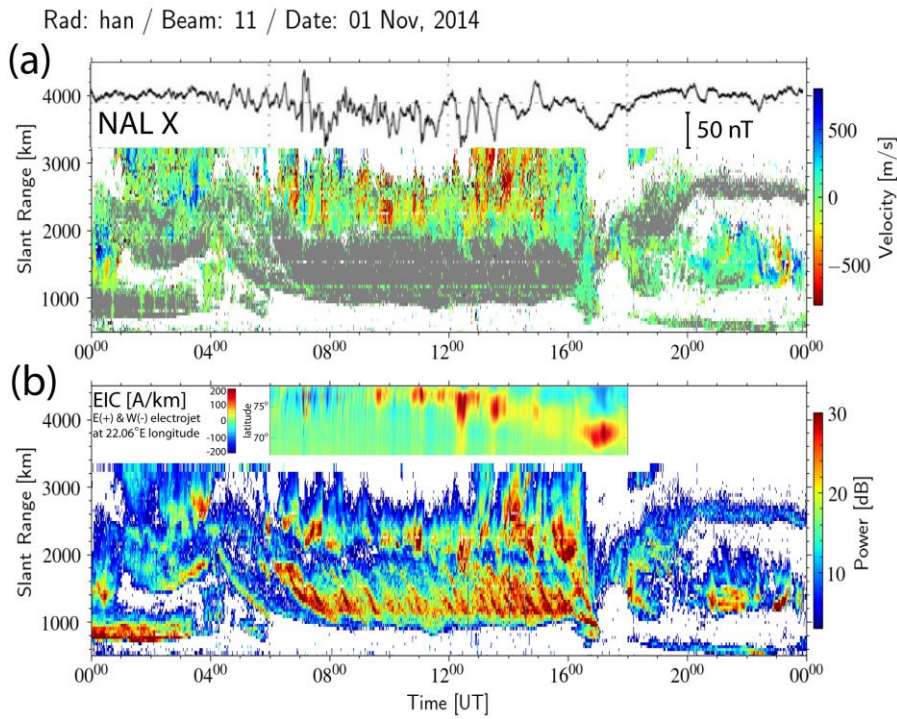


**Figure 5:** (a) The line-of-sight (LoS) velocity and (b) the radar scatter power (ground scatter power shown in grey color in the velocity plot) observed by the Hankasalmi radar beam 11 on November 1, 2014. The X-component of the ground magnetic field perturbations in Ny Ålesund (NAL) is superposed representing the fluctuations of ionospheric currents modulated by solar wind Alfvén waves. 1D equivalent currents estimates that use all IMAGE magnetometers are also superposed.

Rad: han / Beam: 11 / Date: 05 Nov, 2014

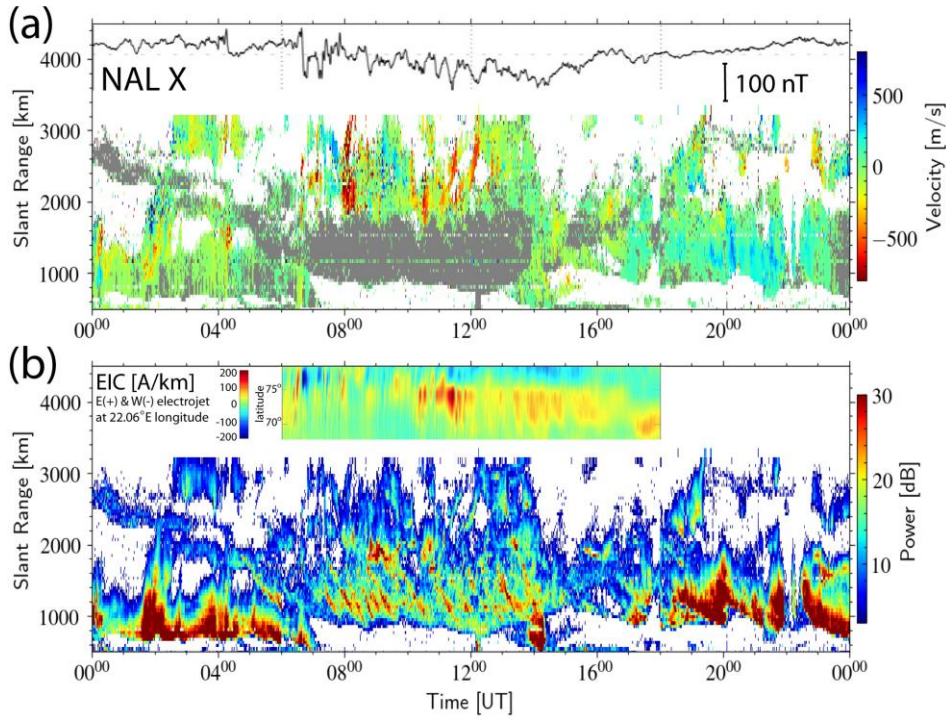


**Figure 6:** The same as Fig. 5 but for November 5, 2014.

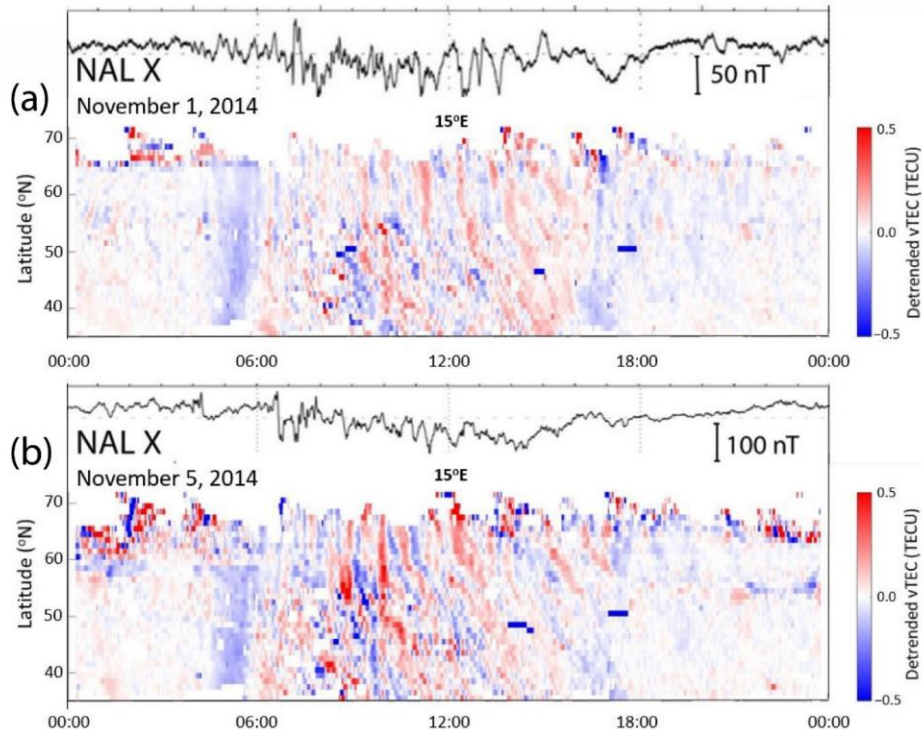


**Figure 7:** The detrended vTEC mapped along longitude of 15°E on (a) November 1 and (b) November 5, 2014. The X-component of the ground magnetic field perturbations in Ny Ålesund (NAL) is superposed.

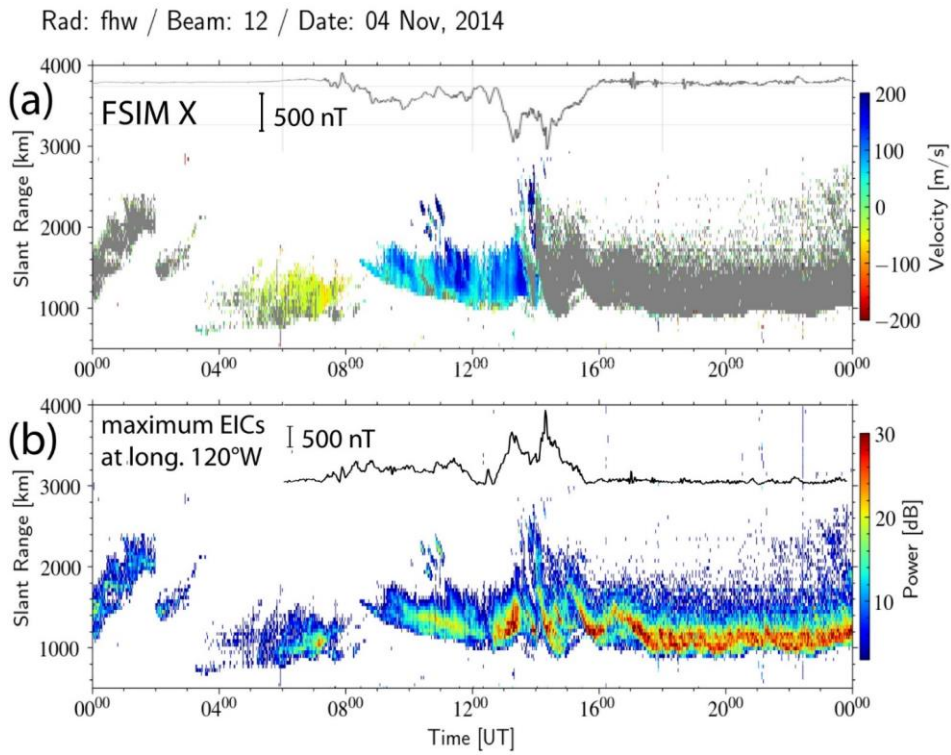


**Figure 8:** (a) The line-of-sight (LoS) velocity and (b) the radar scatter power (ground scatter power shown in grey color in the velocity plot) observed by the Fort Hays West radar beam 12 on November 4, 2014. The X-component of the ground magnetic field perturbations in Fort Simpson (FSIM) and the maximum EICs at longitude 120°W are superposed.

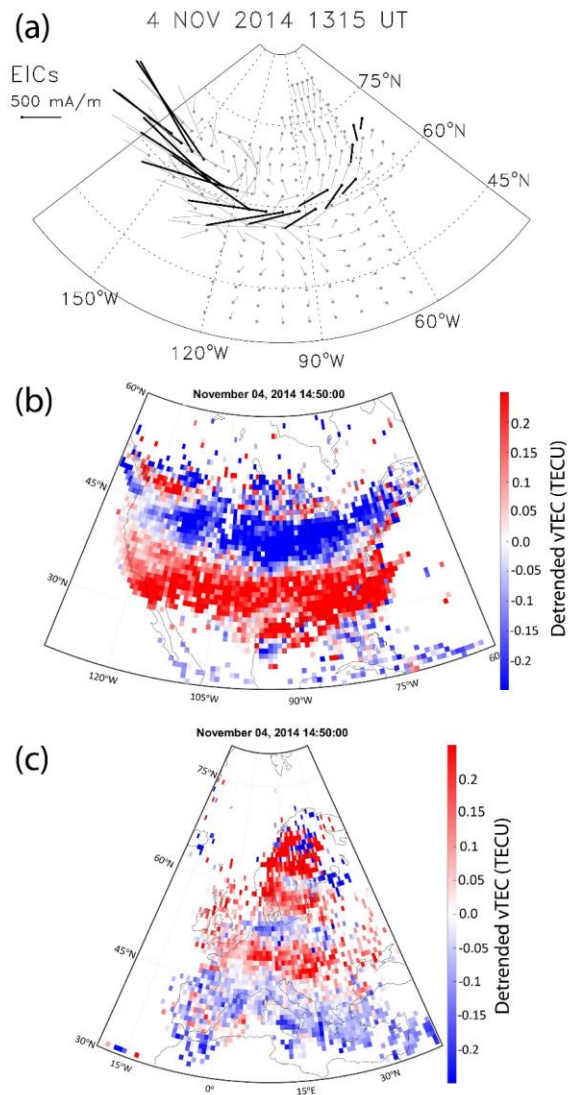


**Figure 9:** (a) The intensification of the westward electrojet over North America, and the detrended vTEC maps over (b) North America and (c) Europe.

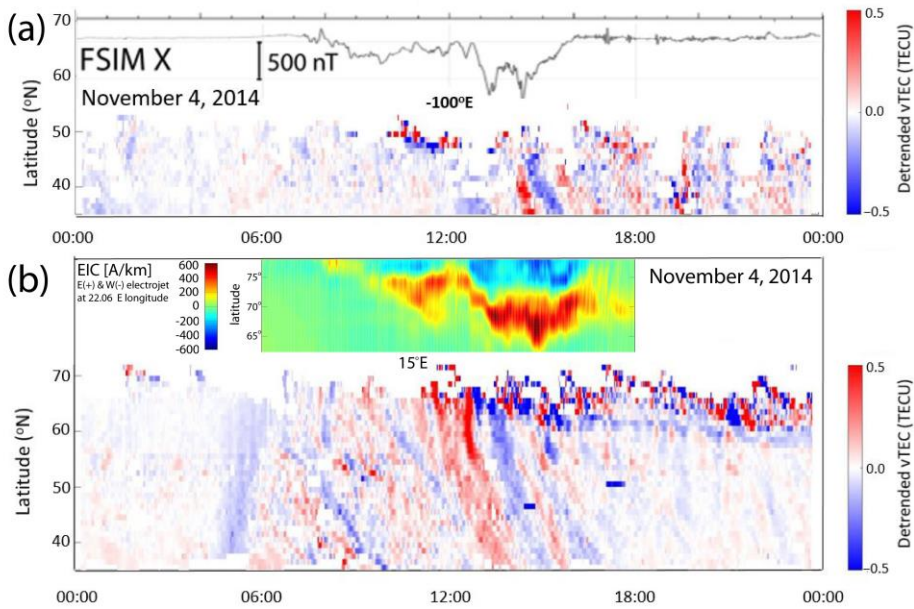


**Figure 10:** The detrended vTEC mapped along longitude of (a) 100°W and (b) 15°E on November 4, 2014. The X-component of the ground magnetic field in Fort Simpson (FSIM) and Hornsund (HOR) are superposed. ID equivalent currents estimates over Scandinavia are superposed.

Formatted: Font: Not Bold

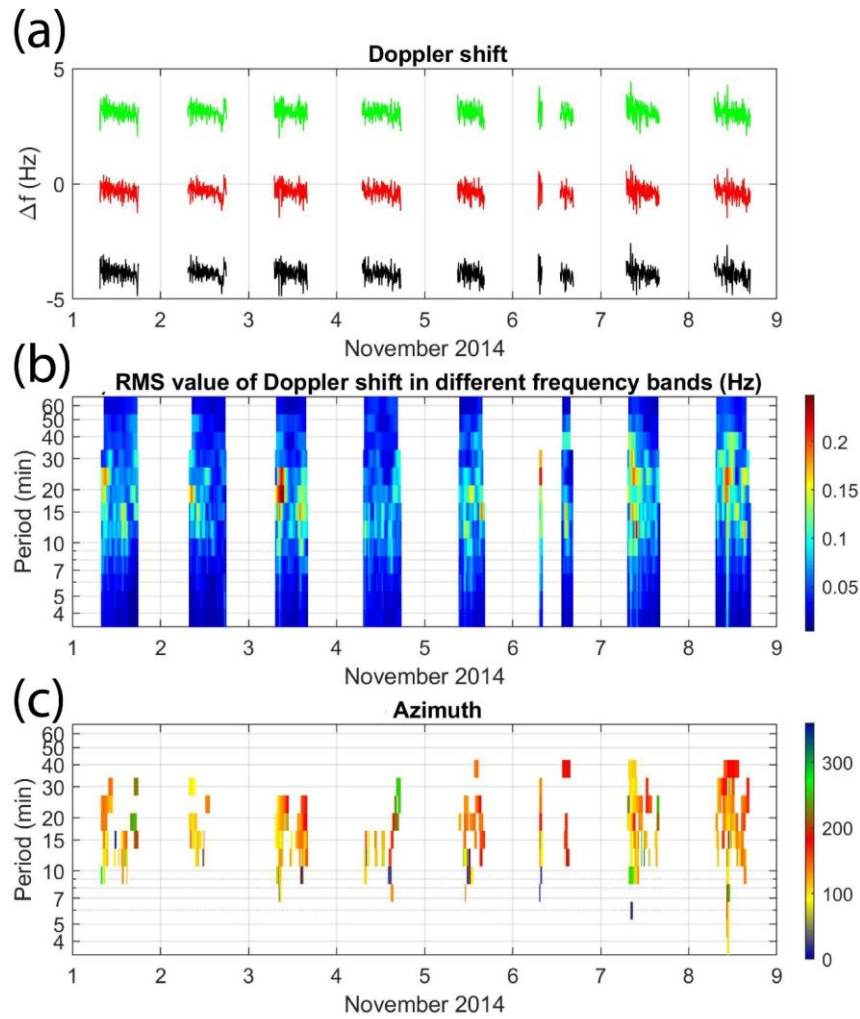


**Figure 11:** (a) Doppler shift frequencies of spectral density maxima for individual transmitter-receiver pairs (including artificial offsets) from X to Y. (b) Dynamic spectra (periodograms) of Doppler shift signals and (c) the propagation azimuth of waves, displayed as function of period and time for November 1-8, 2014.

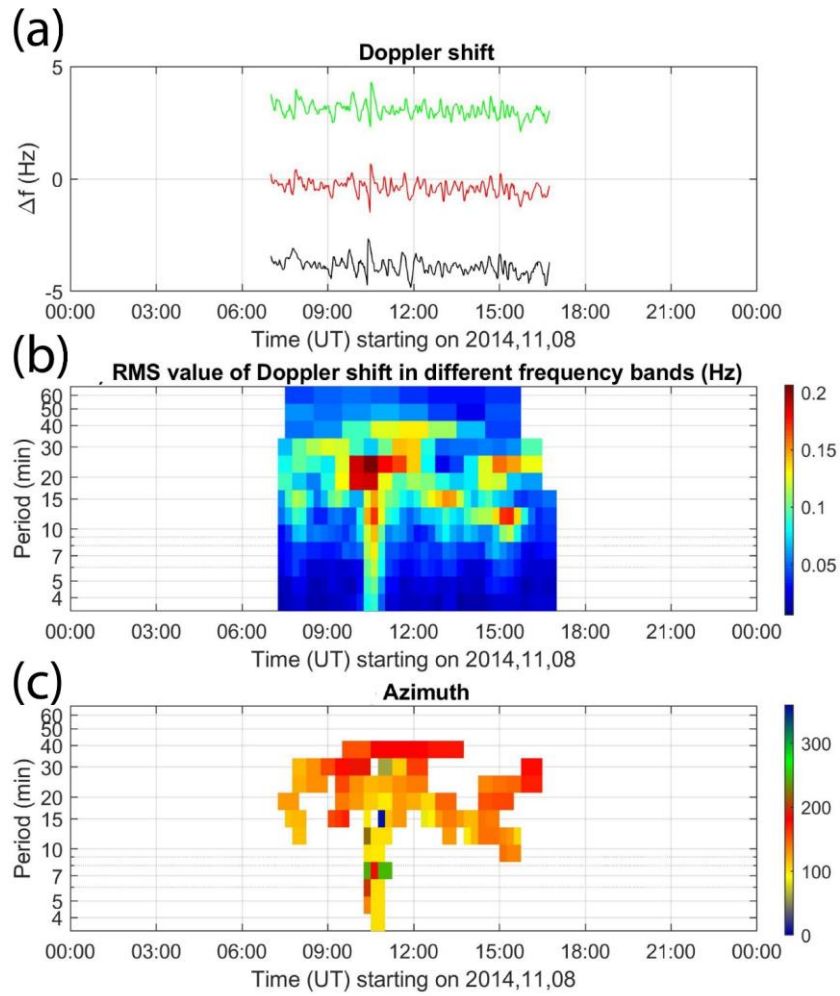


**Figure 12:** The same as Fig. 11 but expanded for November 8, 2014.

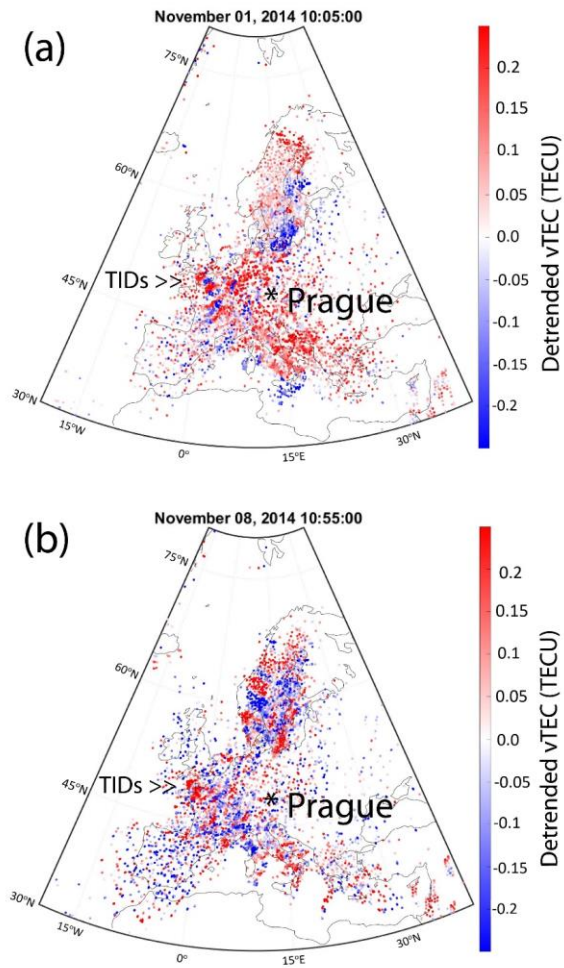


**Figure 13:** The detrended vTEC maps on (a) November 1 and (b) November 8, 2014.

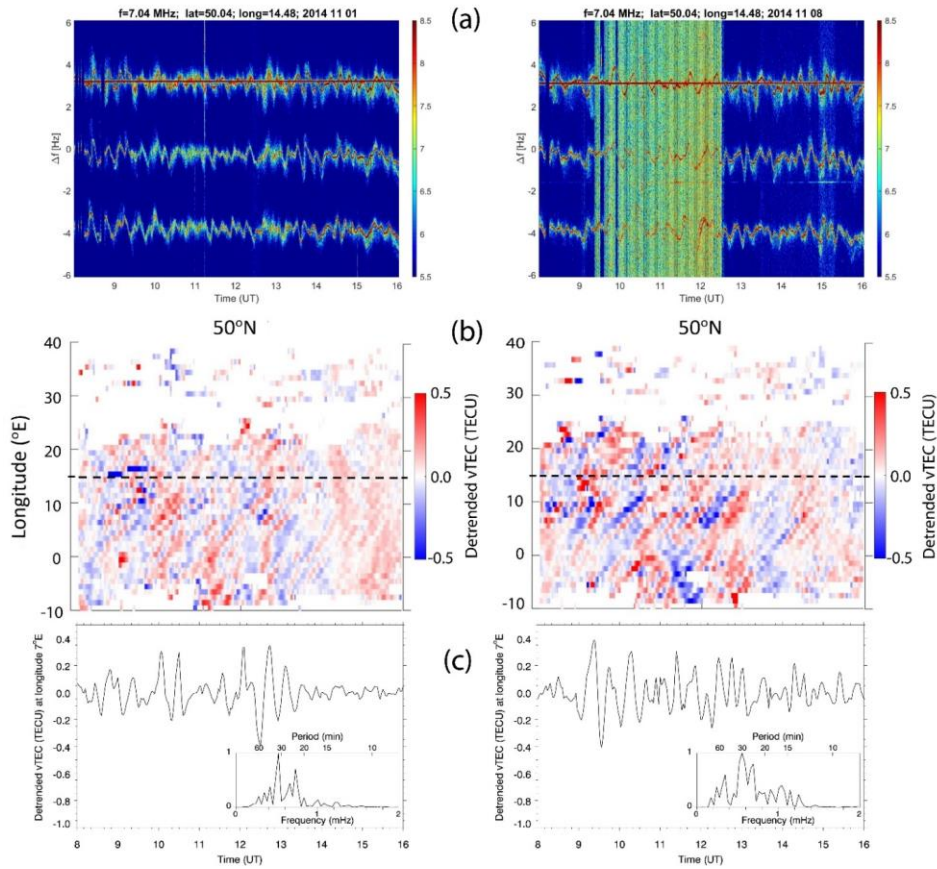


**Figure 14:** (a) The Doppler shift spectrogram recorded at frequency 7.04 MHz on November 1 and 8, 2014. (b) The detrended vTEC mapped along latitude of  $50^\circ N$ . The dashed line shows the longitude of Prague. (c) The detrended vTEC time series at longitude of  $7^\circ E$  and the normalized FFT spectra.

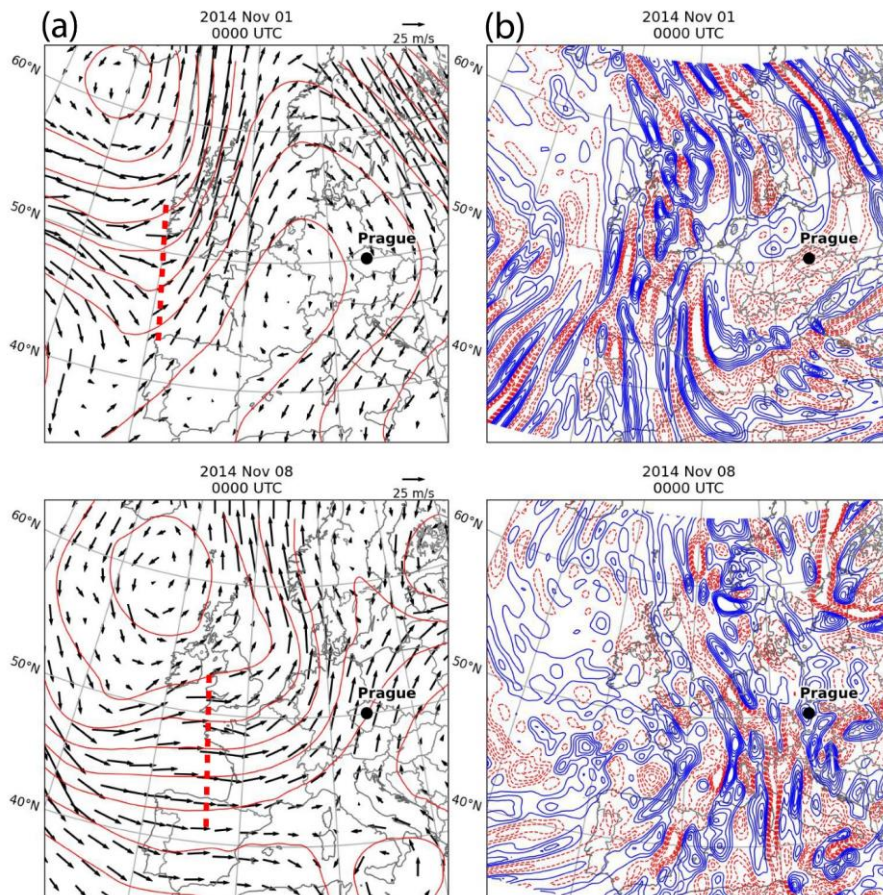


**Figure 15:** (a) The ERA5 geopotential height (red contours at intervals of 100 m), horizontal winds (m/s) at 300-hPa level, with a probable source region of gravity waves indicated by red dashed line. (b) The ERA5 divergence (positive in solid blue line) of the horizontal wind at 150-hPa level, on November 1 and November 8, 2014.